

Light Field Salient Object Detection: A Review and Benchmark

Yao Jiang, Tao Zhou, Ge-Peng Ji, Keren Fu*, Qijun Zhao, and Deng-Ping Fan

Abstract—Salient object detection (SOD) is a long-standing research topic in computer vision and has drawn an increasing amount of research interest in the past decade. Since light fields record more comprehensive and complete information of natural scenes that benefits SOD in a number of ways, using the light field inputs to improve saliency detection over conventional RGB inputs is an emerging trend. This paper provides the first comprehensive review and benchmark for SOD on light field, which has long been lacking in the saliency community. Firstly, we introduce preliminary knowledge on lights, including theory and data forms, and then review existing studies on light field SOD, covering ten traditional models, seven deep learning-based models, one comparative study, and one brief review. Existing datasets for light field SOD are also summarized with detailed information and statistical analyses. Secondly, we benchmark seven representative light field SOD models together with several cutting-edge RGB-D SOD models on four widely used light field datasets, from which insightful discussions and analyses, including a comparison between light field SOD and RGB-D SOD models, are achieved. Besides, due to the inconsistency of datasets in their current forms, we further generate complete data and supplement focal stacks, depth maps and multi-view images for the inconsistent datasets, making them consistent and unified. Our supplemental data makes a universal benchmark possible. Lastly, because light field SOD is quite a special problem attributed to its diverse data representations and high dependency on acquisition hardware, making it differ greatly from other saliency detection tasks, we provide nine hints into the challenges and future directions, and outline several open issues. We hope our review and benchmarking could serve as a catalyst to advance research in this field. All the materials including collected models, datasets, benchmarking results, and supplemented light field datasets will be publicly available on our project site <https://github.com/kerenfu/LFSOD-Survey>.

Index Terms—Light field, salient object detection, deep learning, benchmarking.

I. INTRODUCTION

SALIENT object detection (SOD) [1] is a fundamental task in computer vision, aiming at detecting and segmenting the most human-eye-attracting regions or objects in a scene. SOD is one subfield of saliency detection, with the other being eye fixation prediction [2]–[5], whose goal is to predict where humans look in a scene. SOD plays an important role and has wide applications in computer vision, computer graphics,

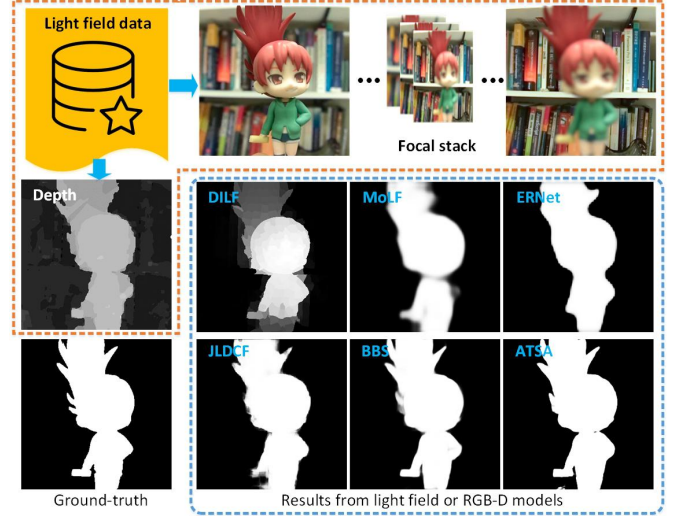


Fig. 1: Salient object detection on a sample scenario using three light field based (*i.e.*, DILF [25], MoLF [26] and ERNet [27]) and three state-of-the-art RGB-D based SOD models (*i.e.*, JLDCE [28], BBS [29], and ATSA [30]).

and robotics. For example, in computer vision, it is used in image retrieval [6], object detection and recognition [7]–[10], semantic segmentation [11]–[13] and unsupervised video object segmentation [14], [15]. In computer graphics, applications include non-photorealist rendering [16], automatic image cropping [17], image re-targeting [18] and video summarization [19], [20]. In robotics, SOD assists human-robot interaction [21], [22] and object discovery [23], [24].

In recent years, deep learning-based SOD has shown great potential, and attracted increasing research interest. However, SOD based on a single modality (*i.e.*, detection on a single RGB input image) still encounters several challenges in complex scenarios with, for instance, heavy background clutter [31], or high similarity between foreground and background. To solve these challenges, incorporating additional supplementary knowledge, such as scene depth [28]–[30], [32]–[37] or motion [38], has been shown to boost SOD performance. In this regard, using light field data [25]–[27], [39]–[54] is another emerging trend.

Light field SOD explores how to detect salient objects using light field data as input. In the 3D space, a light field [55] captures all the light rays at every spatial location and in every direction. As a result, it can be viewed as an array of images captured by a grid of cameras. Compared with the RGB images captured by a regular camera or depth maps

Y. Jiang, K. Fu and Q. Zhao are with the College of Computer Science, Sichuan University, China. (Email: yaojiangyj@foxmail.com, fkrsuper@scu.edu.cn, qjzhao@scu.edu.cn).

T. Zhou and D.-P. Fan are with the Inception Institute of Artificial Intelligence (IIAI), Abu Dhabi, UAE. (Email: taozhou.ai@gmail.com, dengpfan@gmail.com).

G.-P. Ji is with the School of Computer Science, Wuhan University, China. (Email: gepengai.ji@gmail.com)

Corresponding author: Keren Fu.

acquired by a depth sensor, the light field data acquired by a plenoptic camera records more comprehensive and complete information of natural scenes, covering, for example, depth information [56]–[60], focusness cues [39], [60] as well as angular changes [50], [60]. Therefore, light field data can benefit SOD in a number of ways. Firstly, light fields can be refocused after being acquired [60]. This enables a stack of images focusing on different depth to be produced, providing focusness cues that have been demonstrated useful for SOD [61]. Secondly, a light field can provide images of a scene from an array of viewpoints [62]. Such images have abundant spatial parallax and geometric information. Lastly, the depth information of a scene is embedded in light field data and can be estimated from a focal stack or multi-view images by different means, as described in [56]–[59]. In this sense, RGB-D data could be deemed as a special degenerated case of light field data. Fig. 1 shows example results obtained using light field SOD methods as well as RGB-D SOD models on light field data (a focal stack) and depth data.

Although light field data brings great benefits to SOD and first emerged in 2014 [39], this research area still remains underexplored. Specifically, compared with RGB SOD or RGB-D SOD, there are fewer studies on light field SOD. Despite this sparsity of literature, existing models vary in technical frameworks as well as light field datasets used. However, to the best of our knowledge, there is no comprehensive review or benchmark for light field SOD. Although, a comparative study was conducted by Zhang *et al.* [54] in 2015, they only compared the classic light field SOD model proposed by Li *et al.* [39] with a set of 2D saliency models to demonstrate the effectiveness of incorporating light field knowledge. Besides, the evaluation was conducted on the LFSOD dataset, which only contains 100 light field images. Recently, Zhou *et al.* [63] briefly summarized existing light field SOD models and related datasets. However, their work was mainly focused on RGB-D based SOD, and only a small portion of content and space was dedicated to reviewing light field SOD, leading to an insufficient review of model details and related datasets. Besides, they did not benchmark light field SOD models or provide any performance evaluation. Thus, we believe that the lack of a complete review of the existing models and datasets may hinder further research in this field.

To this end, in this paper we conduct *the first comprehensive review and benchmark for light field SOD*. We review previous studies on light field SOD, including ten traditional models [25], [39]–[42], [44]–[48], seven deep learning-based models [26], [27], [49]–[53], one comparative study [54], and one brief review [63]. In addition, we also review existing light field SOD datasets [39], [44], [49], [50], [52], and provide statistical analyses for them, covering object size, distance between the object and image center, focal slice number, and number of objects. Due to the inconsistency of datasets (for example, some do not provide focal stacks, while others lack depth maps or multi-view images), we further generate and complement complete data, including focal stacks, depth maps and multi-view images for some datasets, therefore making them consistent and unified. Besides, we benchmark seven light field SOD models [25]–[27], [39], [40], [50], [52] whose

results/codes are available, together with several cutting-edge RGB-D SOD models [28]–[30], [32]–[37], discussing the connection between the two and providing insight into the challenges and future directions. All the materials involved in this paper, including collected models, benchmark datasets, and results, supplemental light field data, and source code links, will be made publicly available on <https://github.com/kerenfu/LFSOD-Survey>. The main contributions of this paper are four-fold:

- We provide the first systematic review on light field SOD, including models and datasets. Such a survey has long been lacking in the saliency community and is helpful for encouraging future research in this area.
- We conduct analyses on the properties of different datasets. As some datasets lack certain forms of data, *e.g.*, focal stacks, or multi-view images, we generate more data from existing datasets as a supplement, making them more complete and unified. This will also facilitate future research in this area.
- We further benchmark seven light field SOD models together with several cutting-edge RGB-D SOD models on the datasets with our supplemental data, and provide insightful discussions.
- We investigate several challenges for light field SOD and discuss its relation to other topics, shedding light on the challenges and directions for future work.

The remainder of the paper is organized as follows. We review light field preliminaries, existing models and datasets for light field SOD, and provide related discussions and analyses in Section II. In Section III, we describe the evaluation metrics used as well as benchmark results. We then discuss future research directions and outline several open issues of this field in Section IV. Finally, we draw conclusion in Section V.

II. PRELIMINARIES, MODELS AND DATASETS

In this section, we first briefly introduce the theory of light field, the data forms of it, and how it has been used for SOD. We then review the previous works on light field SOD, roughly categorizing them into traditional models and deep learning-based models. Finally, we summarize datasets explored for light field SOD and review their detailed information.

A. Light Field

1) *Light Field and Light Field Cameras*: A light field [55] consists of all the light rays flowing through every point and in every direction of the 3D space. In 1991, Adelson and Bergen [64] proposed a plenoptic function (P), which uses $P(\theta, \phi, \lambda, t, x, y, z)$ to describe the wavelength λ and time t in any direction (θ, ϕ) on any point (x, y, z) , in order to represent the light field information. In an imaging system, the wavelength and time can be represented by RGB channels and different frames, and light usually propagates along a specific path. As a result, Levoy and Hanrahan [65] proposed the two-plane parameterization of the plenoptic function to represent the light field in the imaging system. The two-plane parameterization (L) of the plenoptic function, illustrated in Fig. 2 (b), can be formulated as $L(u, v, x, y)$. In this scheme,

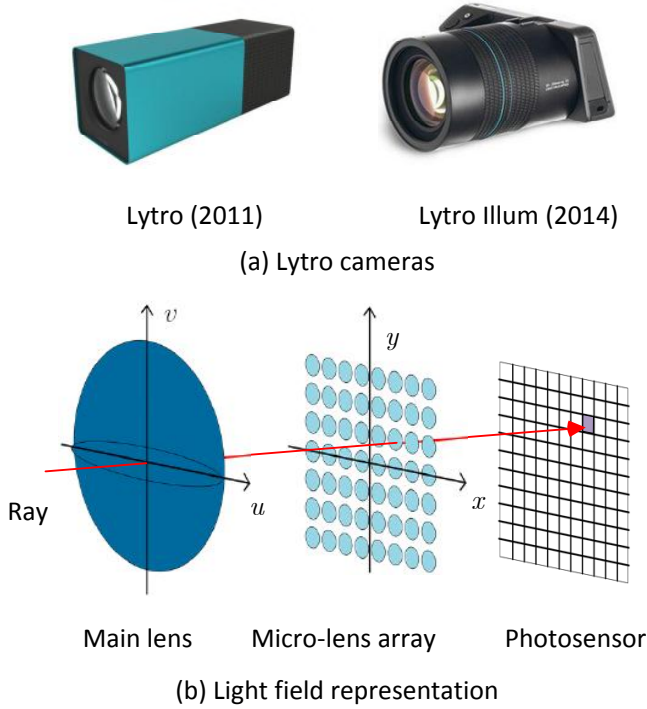


Fig. 2: Lytro cameras (a) and representation of light field (b).

each ray in the light field is determined by two parallel planes to represent spatial (x, y) and angular (u, v) information. Based on this theory, devices that can capture light fields were invented, such as the Lytro camera, shown in Fig. 2 (a). This kind of camera contains a main lens and a micro-lens array placed before the photosensor, where the former serves as the “ uv ” plane, which records the angular information of rays, and the latter serves as the “ xy ” plane, which records the spatial information. Fig. 2 (b) shows the graphical representation of the two-plane parameterization for light field. Due to the above four-dimensional parameterization, data from such a light field is often called 4D light field data [25]–[27], [39]–[54].

2) *Forms of Light Field Data:* Up to now, all light field datasets for SOD have been captured by Lytro cameras, the raw data for which are LFP/LFR files (the former are obtained from Lytro whereas the latter are from Lytro Illum). All images in the current light field datasets were generated by processing LFP/LFR files using Lytro Desktop software¹ or LFToolbox². Since the raw data can hardly be utilized, the data forms of light fields leveraged by existing SOD models are diverse, including focal stacks and all-in-focus images [25]–[27], [39], [40], [42], [44], [46]–[48], [50], [51], multi-view images and center-view images [44], [50], [53], and micro-lens image arrays [41], [52]. As mentioned before, depth images can also be synthesized from light field data [56]–[59], and therefore they can form RGB-D data sources for RGB-D based SOD models (Fig. 1). Focal stacks and all-in-focus images are shown in Fig. 3, whereas multi-view images, center-view images and depth images are shown in Fig. 5.

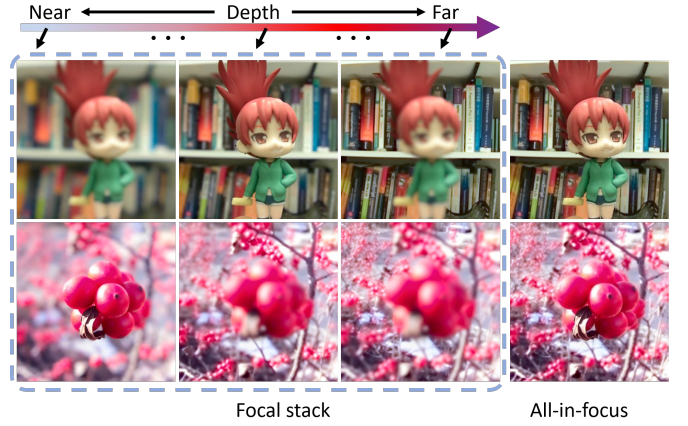


Fig. 3: Focal stacks and all-in-focus images.

Specifically, a focal stack (left three columns in Fig. 3) contains a series of images focusing on different depths. Such images are generated by processing the raw light field data using digital refocusing techniques. The refocusing principle is demonstrated in Fig. 4, which only shows the case of u and x dimensions. Suppose a light ray enters the main lens at location u . If the imaging plane’s position F (F denotes the focal distance of the main lens) is changed to F' , where $F' = \alpha F$, a refocused image can be computed as follows. First, given the 4D light field L_F , the new light field L_α regarding the new imaging plane at F' can be derived as

$$L_\alpha(u, v, x, y) = L_F(u, v, u + \frac{x - u}{\alpha}, v + \frac{y - v}{\alpha}). \quad (1)$$

Next, after obtaining the new light field $L_\alpha(u, v, x, y)$, a refocused image on the imaging plane can be synthesized as

$$I_\alpha(x, y) = \iint L_\alpha(u, v, x, y) du, dv. \quad (2)$$

One can see that by changing the parameter α , a series of refocused images can be generated, composing a focal stack. After the focal stack is obtained, an all-in-focus image can be produced by photo-montage [66]. The algorithm can be summarized as putting all the clear pixels together, where the clarity of pixels can be estimated by the associated gradients. Usually, in-focus pixels should correspond to the largest gradients across the focal stack. More details on the algorithm can be found in [57], [58], [67].

In addition to focal stacks, multi-view images (Fig. 5) can also be derived from light field data. As mentioned before, in the 4D light field representation $L_F(u, v, x, y)$, (u, v) encode the angular information of incoming rays. Thus, an image from a certain viewpoint can be generated by sampling at a specific angular direction (u^*, v^*) , and the image can be represented by $L_F(u^*, v^*, x, y)$. By varying (u^*, v^*) , multi-view images can be synthesized. Specially, when the angular direction (u^*, v^*) is equal to that of the central view, namely (u_0, v_0) , the center-view image is achieved. On the other hand, micro-lens images can be generated by sampling the (x, y) dimensions. Providing a micro-lens location (x^*, y^*) leads to a micro-lens image $L_F(u, v, x^*, y^*)$, which captures multiple perspectives of a scene point. Note that, by varying (x^*, y^*) ,

¹<http://lightfield-forum.com/lytro/lytro-archive/>

²<http://code.behnam.es/python-lfp-reader/> and also <https://www.mathworks.com/matlabcentral/fileexchange/75250-light-field-toolbox>

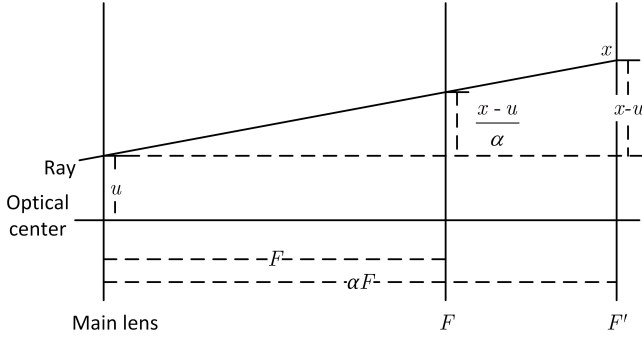


Fig. 4: Illustration of the refocus principle.

different micro-lens images can be obtained, which together compose a micro-lens image array representing complete light field information. A visualization of micro-lens and multi-view images can be found in the recent work [52].

Moreover, depth maps containing scene depth information can also be estimated from a light field. As mentioned, depth information is embedded in the focusness and angular cues, so a depth map can be generated by combining both defocusness and correspondence (angular) cues. For more details on depth estimation from light fields please refer to [56]–[59].

B. Light Field SOD Models and Reviews

In this section, we review existing models proposed for light field SOD, including ten traditional models that employ hand-crafted features, and seven deep learning-based models. Also, one comparative study and one brief review are revisited. Details of all these works are summarized in Table I.

1) Traditional Models:

LFS [39] was the pioneering (and earliest) work on light field SOD, which started to investigate the problem of using light field data, instead of conventional RGB images or depth maps as input for SOD. Together with this method, the first light field SOD dataset was constructed. LFS first incorporated the focusness measure with location priors to determine the background and foreground slices. Then, in the all-focus³ image, it computed the background prior and contrast cues to detect saliency candidates. Finally, a saliency map was generated by incorporating the saliency candidates in the all-focus image with those in the foreground slices, where objectness cues were used to weight the candidates. An extension of this work was published in [43].

WSC [40] was proposed as a unified framework for 2D, 3D and light field SOD problems, which can handle heterogeneous data. Based on the weighted sparse coding framework, the authors first used a non-saliency dictionary to reconstruct a reference image, where patches with high reconstruction error were selected as the saliency dictionary. This saliency dictionary was later refined by iteratively running the weighted sparse framework to achieve the final saliency map. For the light field case, features used for dictionary construction were

³In this paper, “all-focus” and “all-in-focus” are used interchangeably. Their meanings are the same.

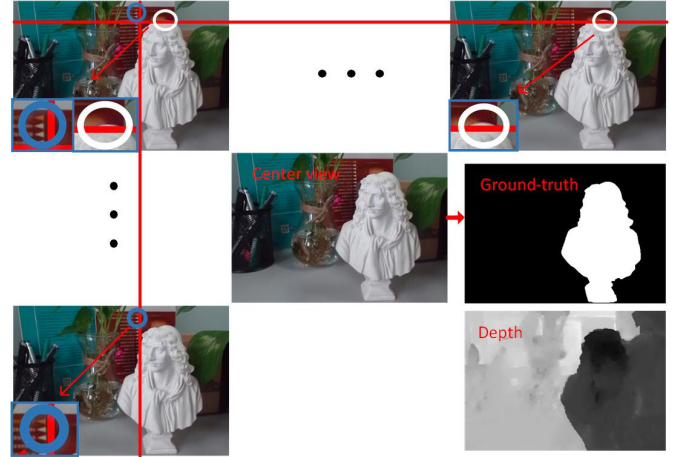


Fig. 5: Multi-view images (including the center-view image), the depth map, and the ground-truth. Notice the inconspicuous parallax (disparity) conveyed by the multi-view images (zoomed in as the bottom-left in each multi-view image).

derived from the all-focus RGB image, depth map, and also focal stacks.

DILF [25] used global cues in the light field data to measure the saliency of a superpixel. It computed the depth-induced contrast saliency and color contrast saliency from the all-focus image and depth image, which were then used to generate a contrast saliency map. It also computed the background priors based on the focusness measure embedded in the focal stacks and used them as weights to eliminate background distraction and enhance the saliency estimation.

RL [41] proposed to estimate the relative locations of scene points using a filtering process. It designed two filters, namely the foreground and background filter, to calculate the relative locations in a raw light field image. Such relative locations, which can be treated as conveying scene depth information, were then incorporated with the robust background detection and saliency optimization framework proposed in [68] to achieve enhanced saliency detection.

BIF [42]. This work used the Bayesian framework to fuse multiple features extracted from RGB images, depth maps and focal stacks. Inspired by traditional SOD methods, this method utilized a boundary connectivity prior, background likelihood scores and color contrast to generate background probability maps, foreground slices, color-based saliency maps and depth-induced contrast maps. For all the features extracted, it then used a two-stage Bayesian scheme to fuse diverse features.

MA [44] measured the saliency of a superpixel by computing the intra-cue distinctiveness between two superpixels, where features considered include color, depth, and flow inherited from different focal planes and multiple viewpoints. The light-field flow was first employed in this method, estimated from focal stacks and multi-view sequences, to capture depth discontinuities/contrast. The saliency measure was later enhanced using a location prior and a random-search-based weighting strategy. In addition, the authors proposed a new light field SOD dataset, which was the largest at that time.

SDDF [45] made use of depth information embedded

TABLE I: Overview of light field SOD models and review works. For datasets, please see Table II. We use the following abbreviations: FS=focal stacks, DE=depth maps, MV=multi-view images, ML=micro-lens images, OP=open-source. FS, DE, MV and ML indicate the data forms input to the models. Emerged datasets are highlighted in **bold** in the “Main components”.

	Models	Pub.	Year	Training dataset(s)	Testing dataset(s)	Main components	FS	DE	MV	ML	OP
Traditional models	LFS [39]	CVPR	2014	-	LFSD	Focusness measure, location priors, contrast cues, background prior, new dataset	✓				✓
	WSC [40]	CVPR	2015	-	LFSD	Weighted sparse coding, saliency/non-saliency dictionary construction	✓				✓
	DILF [25]	IJCAI	2015	-	LFSD	Depth-induced/Color contrast, background priors by focusness	✓	✓			✓
	RL [41]	ICASSP	2016	-	LFSD	Relative locations, guided filter, micro-lens images				✓	
	BIF [42]	NPL	2017	-	LFSD	Bayesian framework, boundary prior, color/depth-induced contrast	✓	✓			
	LFS [43]	TPAMI	2017	-	LFSD	An extension of [39]	✓				✓
	MA [44]	TOMM	2017	-	LFSD + HFUT	Superpixels intra-cue distinctiveness, light-field flow, new dataset	✓	✓	✓		
	SDDF [45]	MTAP	2018	-	LFSD	Background priors, gradient operator, color contrast, local binary pattern histograms	✓				
	SGDC [46]	CVPR	2018	-	LFSD	Focusness cues, color and depth contrast	✓	✓			
	RDFD [47]	MTAP	2020	-	LFSD	Region-based depth feature descriptor, dark channel prior, multi-layer cellular automata	✓				
	DCA [48]	TIP	2020	-	LFSD	Depth-induced cellular automata, object-guided depth	✓	✓			
Deep learning models	DLLF [49]	ICCV	2019	DUT-LF	LFSD + DUT-LF	VGG-19, attention subnetwork, ConvLSTM, adversarial examples, new dataset	✓				
	DLSD [50]	IJCAI	2019	DUT-MV	DUT-MV	View synthesis network, multi-view detection/attention, VGG-19, new dataset			✓		✓
	MoLF [26]	NIPS	2019	DUT-LF	HFUT + LFSD + DUT-LF	VGG-19, memory-oriented spatial fusion, memory-oriented feature integration	✓				✓
	ERNet [27]	AAAI	2020	DUT-LF + HFUT	HFUT + LFSD + DUT-LF	VGG-19, ResNet-18, multi-focusness recruiting/screening modules, distillation	✓				✓
	LFNet [51]	TIP	2020	DUT-LF	HFUT + LFSD + DUT-LF	VGG-19, refine unit, attention block, ConvLSTM	✓				
	MAC [52]	TIP	2020	Lytro Illum	Lytro Illum + HFUT + LFSD	Micro-lens images/image arrays, DeepLabv2, model angular changes, new dataset				✓	✓
	MTCNet [53]	TCSVT	2020	Lytro Illum	Lytro Illum + HFUT	Edge detection, depth inference, feature-enhanced salient object generator			✓		
Reviews	CS [54]	NEURO	2015	-	LFSD	Comparative study between 2D vs. light field saliency					
	RGBDS [63]	CVM	2020	-	-	In-depth RGB-D SOD survey, brief review of light field SOD					

in focal stacks to conduct accurate saliency detection. A background measurement was first obtained by applying a gradient operator to focal stack images, and the focal slice with the highest measurement was chosen as the background layer. A coarse prediction was generated by separating the background and foreground in the all-focus image using the derived background regions, and the final saliency map was calculated globally via both color and texture (local binary pattern histograms) contrast based on the coarse saliency map.

SGDC [46]. This work presented a light field SOD approach named contrast-enhanced saliency detection for optimizing the multi-layer light field display. It first computed a super-pixel level focusness map for each refocused image and then chose the refocused image with the highest background likelihood score to derive background cues. Such focusness background cues were later incorporated with color and depth contrast saliency. The final results were optimized by the optimization framework proposed in [68].

RDFD [47] addressed the light field SOD problem via a multi-cues integration framework. A region-based depth feature descriptor (RDFD) defined over the focal stack was

proposed, which was based on the observation that dark channel priors can be used to estimate the degree of defocusing/blurriness. The RDFD was generated by integrating the degrees of defocusing over all focal stack images, alleviating the limitation of requiring accurate depth maps. RDFD features were used to compute a region-based depth contrast map and a 3D spatial distribution prior. These cues were merged into a single map using a multi-layer cellular automata (MCA).

DCA [48]. As a recent work, this paper proposed a depth-induced cellular automata (DCA) for light field SOD. The inputs of the model included an all-focus image, a depth map and a focal stack. Firstly, it used the focusness and depth cue to calculate the object-guided depth map and select background seeds. Based on the seeds, a contrast saliency map was computed and multiplied with the object-guided depth map to achieve a depth-induced saliency map, which was subsequently optimized by DCA. Finally, the optimized map was combined with the depth-induced saliency map, and a Bayesian fusion strategy and CRF were employed to further refine the result.

Summary of Traditional Models. As summarized in Ta-

ble I, traditional SOD models using light fields often extend various handcrafted features/hypotheses widely adopted in conventional saliency detection, such as color contrast, background priors, and object location cues. Some features specially tailored for light fields, like focusness, depth, and light-field flow, are also considered. Besides, these models tend to employ post-refinement steps, *e.g.*, an optimization framework [25], [41], [44], [46], [48] or CRF [48], to obtain saliency maps with more accurate boundaries. Despite this, due to the general limitations of using handcrafted features, traditional SOD models can hardly generalize well to challenging scenarios. Regarding the data forms leveraged, almost all traditional models work with focal stacks, while depth is incorporated by some of them, and very few consider the multi-view [44] and micro-lens data [41] from the light field. Further, due to the dataset limitations in the early times, most traditional models are only evaluated on the LFSD dataset.

2) Deep Learning-Based Models:

DLLF [49]. This paper proposed a two-stream fusion framework which explored focal stacks and all-in-focus images separately. In the focal stack stream, DLLF first extracted features from cascaded focal slices through a fully convolutional network. Diverse features from different slices were then integrated by a recurrent attention network, which employed an attention subnetwork and ConvLSTM [69] to adaptively incorporate weighted features of slices and exploit their spatial relevance. Finally, the fused features were fed to convolutional layers to generate a saliency map for the focal stack stream. This map was combined with the other saliency map derived from the all-in-focus image to generate the final saliency map. In addition, to improve the robustness of the proposed network, the authors generated adversarial examples by adding noise to the training images. In addition, to address the limitation of data for training deep networks, a new large dataset was introduced for light field SOD.

DLSO [50] treated light field SOD as two subproblems: light field synthesis from a single-view image and light-field-driven SOD. This model first employed a light field synthesis network, which estimated depth maps along the horizontal and vertical directions with two independent convolutional networks. According to the depth maps, the single-view image was warped into horizontal and vertical viewpoints of the light field. After the light field images were constructed, a light-field-driven SOD network, consisting of a multi-view saliency detection subnetwork and multi-view attention module, was designed for saliency prediction. Specifically, this model inferred a saliency map from a 2D single-view image, but utilized the light field (the multi-view data form) as the middle bridge. To train the model, a new dataset containing multi-view images and a pixel-wise ground-truth of central view was introduced.

MoLF [26]. To better exploit spatial information and comprehensively integrate multi-level features, the authors proposed a memory-oriented spatial fusion module (Mo-FSM) and feature integration module (Mo-FIM). Mo-FSM utilized an attention mechanism to learn the importance of different feature maps and a ConvLSTM [69] to gradually refine the spatial information. A global perception module (GPM) was

used to capture global contextual information of the fused feature maps. For Mo-FIM, a scene context integration module (SCIM) and ConvLSTM [69] were employed to learn channel attention maps and exploit their spatial information. Besides, MoLF extracted the focal stack and all-in-focus image features with two separate networks.

ERNet [27]. The computation-and-memory issue is an urgent problem in light field SOD since high-dimensional light field data is used. To address this, the authors proposed a two-stream teacher-student network based on knowledge distillation. The teacher stream used a multi-focusness recruiting module (MFRM) and a multi-focusness screening module (MFSM) to recruit and distill knowledge from focal slices, while the student network took a single RGB image as input for computational efficiency. In this scheme, the student stream was supervised by the saliency maps obtained from the teacher.

LFNet [51]. In this paper, the authors proposed a two-stream fusion network to better refine the complementary information and integrate the focusness and blurriness information, which changed gradually in focal slices. LFNet used two separate networks to extract features from the all-focus image and focal stack, and fed those features to a light field refinement module (LFRM) and integration module (LFIM) to generate a final saliency map. In LFRM, feature maps extracted from a single focal slice were fed to a refinement unit to learn the residuals. Then, they were fused with the all-in-focus features to refine the saliency map using the supplementary information from the focal stack and all-focus image. LFIM used an attention block to adaptively incorporate features of each slice with different weights, and a ConvLSTM [69] to exploit the spatial relevance of the attentive features.

MAC [52] was proposed as an end-to-end deep convolutional network for light field SOD with micro-lens image arrays as input. Firstly, It adopted a MAC (Model Angular Changes) block tailored to model angular changes in each local micro-lens image and then fed the extracted features to a modified DeepLab-v2 [70] network, capturing multiscale information and long-range spatial dependencies. Specifically, the authors proposed three variants of MAC blocks, and showed that, the one with a kernel size the same as the angular resolution achieved the best performance. Together with the model, a new Lytro Illum dataset including high-quality micro-lens image arrays was proposed.

MTCNet [53] proposed a two-stream multi-task collaborative network, consisting of a saliency-aware feature aggregation module (SAFA) and multi-view inspired depth saliency feature extraction (MVI-DSF) module, to extract representative saliency features with the aid of the correlation mechanisms across edge detection, depth inference and salient object detection. SAFA simultaneously extracted focal-plane, edge and heuristic saliency features from a center-view image, while MVI-DSF inferred depth saliency features from a set of multi-view images. Finally, MTCNet combined the extracted features with a feature-enhanced saliency generator to obtain the final saliency map.

Summary of Deep Models. As summarized in Table I, most deep models take a focal stack as network input. Due to the multi-variable property of focal stacks, modules such

TABLE II: Overview of light field SOD datasets. We use the following abbreviations: MOP=multiple-object proportion (the percentage of images in the entire dataset that have more than one object per image), FS=focal stacks, DE=depth maps, MV=multi-view images, ML=micro-lens images, GT=ground-truth, Raw=raw light field data. Here, FS, MV, DE, ML, GT and Raw indicate the data forms provided by the datasets.

Dataset	Scale	Spatial resolution	Angular resolution	MOP	FS	MV	DE	ML	GT	Raw	Device
LFSD [39]	100 (No official split)	360×360	-	0.04	✓		✓		✓	✓	Lytro
HFUT [44]	255 (No official split)	328×328	7×7	0.29	✓	✓	✓		✓		Lytro
DUT-LF [49]	1462 (1000 train, 462 test)	600×400	-	0.05	✓		✓		✓		Lytro Illum
DUT-MV [50]	1580 (1100 train, 480 test)	400×590	7×7	0.04		✓			✓		Lytro Illum
Lytro Illum [52]	640 (No official split)	540×375	9×9	0.15				✓	✓	✓	Lytro Illum

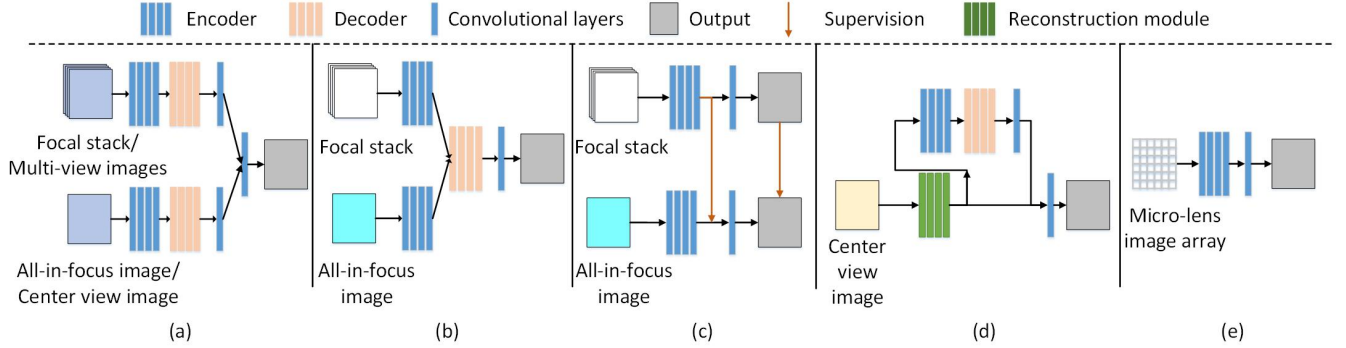


Fig. 6: Frameworks of deep light field SOD models. (a) Late-fusion (DLLF [49], MTCNet [53]). (b) Middle-fusion (MoLF [26], LFNet [51]). (c) Knowledge distillation-based (ERNet [27]). (d) Reconstruction-based (DLSD [50]). (e) Single-stream (MAC [52]). Note that (a) utilizes the focal stack/multi-view images and all-focus/center view image, while (b)-(c) utilize the focal stack and all-focus image. (d)-(e) utilize the center-view image and micro-lens image array.

as attention mechanisms [26], [27], [49]–[51] and ConvLSTMs [26], [27], [49], [51] are preferred. Some deep models consider other data forms beyond focal stacks, such as multi-view images [50], [53] and micro-lens image arrays [52], which often leads to different network designs. The limitation of datasets has been somewhat alleviated in the deep learning era, as three new datasets have been introduced to better train deep neural networks.

Since using deep learning-based schemes for light field SOD is the leading trend, we divided existing deep models into five categories, as illustrated in Fig. 6. The late-fusion scheme (Fig. 6 (a)) aims at obtaining individual predictions from the input focal stack/multi-view images and all-focus/center view image, and then simply fuses the results. The middle-fusion strategy (Fig. 6 (b)) extracts features from the focal stack and all-focus image in a two-stream manner. Fusion across features is done by an elaborately designed decoder. The knowledge distillation-based scheme (Fig. 6 (c)) uses both the features and prediction from the focal stack stream to supervise those features and prediction obtained from the all-focus stream, effectively boosting the performance of the latter. The reconstruction-based models (Fig. 6 (d)) reconstruct light field data/information from a single input image. With the assistance of the reconstructed light field, an encoder-decoder architecture is adopted to complete light field SOD. Finally, the single-stream scheme (Fig. 6 (e)) processes the micro-lens image array directly using a single bottom-up stream to obtain the final prediction.

3) Other Review Works:

CS [54]. This paper provided a comparative study between

light field saliency and 2D saliency, showing the advantage of conducting the SOD task on light field data over single 2D images. It compared the classical model LFS [39] with eight 2D saliency models on the LFSD dataset [39]. Five evaluation metrics were used in the paper to show that the light field saliency model achieved better and more robust performance than models that are based on conventional 2D images.

RGBDS [63]. This paper conducted an in-depth and comprehensive survey on RGB-D salient object detection. It reviewed existing RGB-D SOD models from various perspectives, as well as the related benchmark datasets in detail. Considering the fact that light fields can also provide depth maps, the authors also briefly reviewed the light field SOD models and datasets. However, because the main focus of this paper was RGB-D SOD, only a small part of contents and space was arranged for reviewing light field SOD, and no associated benchmarking was conducted.

C. Light Field SOD Datasets

At present, there are five datasets introduced for the light field SOD task, including LFSD [39], HFUT [44], DUT-LF [49], DUT-MV [50], and Lytro Illum [52]. We summarize details of these datasets in Table II and show some samples from four datasets (*i.e.*, LFSD, HFUT, Lytro Illum, and DUT-LF) in Fig. 7. A brief introduction is given as follows:

LFSD⁴ [39] was the first light field dataset collected for SOD, and contains 60 indoor and 40 outdoor scenes. This dataset was captured by a Lytro camera and provides a focal

⁴<https://sites.duke.edu/nianyi/publication/saliency-detection-on-light-field/>

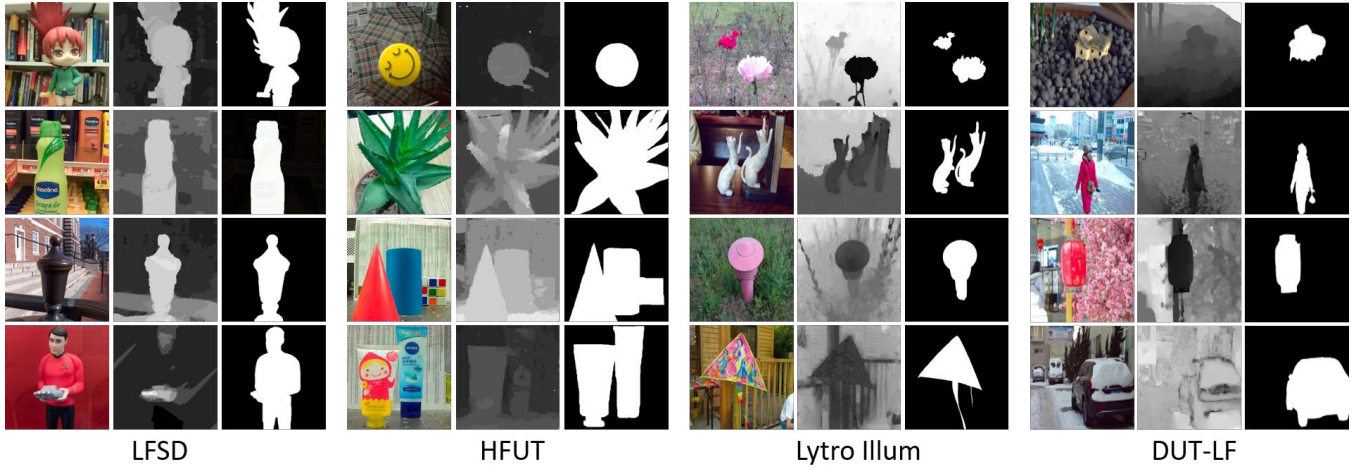


Fig. 7: Examples of RGB images, depth maps, and ground-truths (GTs) from four datasets: LFSD [39], HFUT [44], Lytro Illum [52] and DUT-LF [49]. In each group, RGB images, depth maps and GTs are shown from left to right.

stack, all-in-focus image, depth map and the corresponding ground-truth for each light field. The image spatial resolution is 360×360 . Besides, raw light field data is also available in LFSD. Note that most images in this dataset contain one single center-placed object with relatively simple background.

HFUT⁵ [44] contains 255 light fields for both indoor and outdoor scenes. Each light field contains a focal stack whose slice numbers vary from 1 to 12. The angular resolution is 7×7 and the spatial resolution is 328×328 . Notably, focal stacks, all-in-focus images, multi-view images and coarse depth maps are all provided in this dataset. Several challenges regarding SOD, *e.g.*, occlusions, cluttered background and appearance changes, are present in HFUT.

DUT-LF⁶ [49] is one of the largest light field SOD datasets to date, containing 1,462 light fields in total. It was acquired by a Lytro Illum camera in both indoor and outdoor scenes. The entire dataset is officially divided into 1,000 training samples and 462 testing samples. All-focus images, focal stacks and the corresponding ground-truth are provided for different light fields. The slice number of a focal stack ranges from 2 to 12, and the image spatial resolution is 600×400 . It is worth nothing that DUT-LF covers various challenges, including different types of objects, low appearance contrast between salient objects and their background, and varied object locations.

DUT-MV⁷ [50] is another large-scale light field dataset for SOD, which was generated from the same database as DUT-LF (with 1,081 identical scenes). In contrast to other datasets, this dataset was proposed to better exploit the angular cues. Therefore, only multi-view images with respect to horizontal and vertical viewpoints are available, together with the ground-truth of the center view image. DUT-MV contains 1,580 light fields in total, and is officially divided into training and test sets with 1,100 and 480 samples, respectively. The spatial

resolution of each image is 400×590 and the angular resolution is 7×7 .

Lytro Illum⁵ [52] contains 640 high-quality light fields captured by a Lytro Illum camera. The images in this dataset vary significantly in object size, texture, background clutter and illumination. Lytro Illum provides center-view images, micro-lens image arrays, raw light field data, as well as the corresponding ground-truths of the center-view images. The resolution of micro-lens image arrays is 4860×3375 , while center-view images and ground-truths have a 540×375 spatial resolution. The angular resolution can be inferred as 9×9 .

Dataset Analysis. From the summarization in Table II, we can observe that two issues existed in current datasets, namely scale limitations and non-unified data forms. Compared to the large datasets constructed for the conventional SOD task, such as DUT-OMRON (5,168 images) [71], MSRA10K (10,000 images) [1] and DUTS (15,572 images) [72], the existing light field SOD datasets are still small, making it difficult to evaluate data-driven models and train deep networks. Besides, their data forms are not always identical. For example, Lytro Illum does not provide focal stacks, while DUT-LF/DUT-MV only provide focal stacks/multi-view images without offering the raw data. This makes comprehensive benchmarking very difficult, because a model using focal stacks as input cannot run on DUT-MV and Lytro Illum. We will show how we alleviate this problem in Section III-B, and discuss the underlying future directions in Section IV.

To better understand the above-mentioned datasets, we have conducted statistical analyses, including size ratios of salient objects, distributions of normalized object distances from image centers, numbers of focal slices and numbers of objects. The quantitative results are shown in Fig. 8 and Fig. 9. From Fig. 8 (a), we can see that most objects from these datasets have size ratios lower than 0.6. HFUT and Lytro Illum have relatively small objects, while LFSD has objects that are relatively large in size. Fig. 8 (b) and Fig. 9 clearly show the spatial distributions of objects. From Fig. 9, we can see that all five datasets present strong center bias, and Fig. 8 (b) reveals that objects from Lytro Illum are generally the closest to the

⁵<https://github.com/pencilzhang/MAC-light-field-saliency-net>

⁶https://github.com/OIPLab-DUT/ICCV2019_DeepLightfield_Saliency

⁷<https://github.com/OIPLab-DUT/IJCAI2019-Deep-Light-Field-Driven-Saliency-Detection-from-A-Single-View>

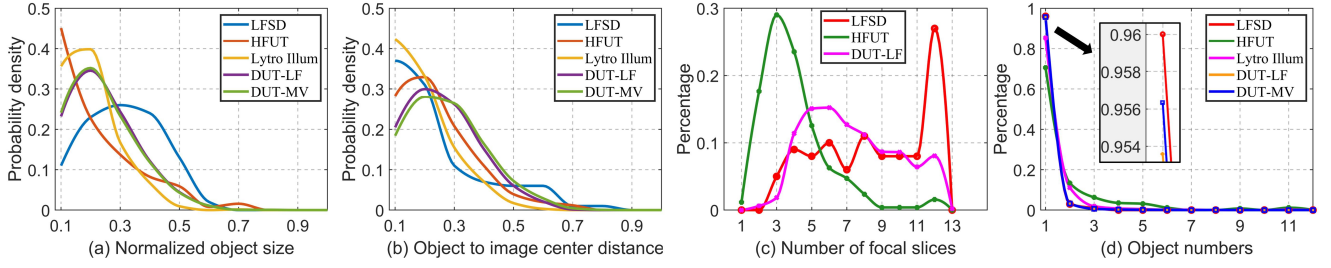


Fig. 8: Statistics of light field datasets, including LFSD [39], HFUT [44], Lytro Illum [52], DUT-LF [49] and DUT-MV [50]. From left to right: (a) distribution of the normalized object size, (b) distribution of the normalized distance between the object and image center, (c) statistics on focal slice numbers, and (d) statistic on object numbers.

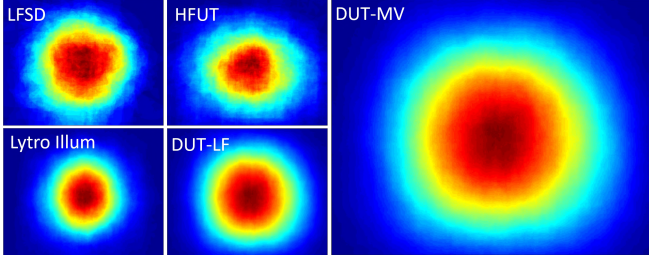


Fig. 9: Object location distribution maps of five datasets (warmer color means higher probability). The maps are computed by averaging ground-truth masks.

image centers (also indicated by Fig. 9).

In addition, the statistics on focal slice numbers are given in Fig. 8 (c). Note that only three datasets, namely LFSD, HFUT, and DUT-LF, provide focal slices. The numbers of slices vary from 1 to 12 and there are notable differences between different datasets. The slice numbers corresponding to the distribution peaks on LFSD, HFUT and DUT-LF are 12, 3, and 6, respectively. This is because LFSD provides richer depth information than the other datasets. Besides, all three datasets have various slices numbers, indicating that a light field SOD model using focal stacks should be able to handle various numbers of input slices. Lastly, from Fig. 8 (d), we can see that most images from these datasets have a single object. Also, HFUT and Lytro Illum have some images with multiple objects (with higher “MOP” in Table II), which could be useful for validating models on detecting multiple objects.

III. MODEL EVALUATION AND BENCHMARK

In this section, we first review five popular evaluation metrics, and then provide a pipeline for achieving dataset unification. Moreover, we carry out a benchmarking evaluation and provide an experimental result analysis.

A. Evaluation Metrics

In our benchmarking of light field SOD models, we employ eight metrics, which are universally agreed upon and are described as follows:

Precision-recall (PR) [1], [4], [73] curve is defined as:

$$Precision(T) = \frac{|M^T \cap G|}{|M^T|}, Recall(T) = \frac{|M^T \cap G|}{|G|}, \quad (3)$$

where M^T is a binary mask obtained by thresholding the saliency map with threshold T , and $|\cdot|$ is the total area of the mask. G denotes the ground-truth. A comprehensive precision-recall curve is obtained by changing T from 0 to 255.

F-measure (F_β) [1], [4], [73] is defined as the harmonic-mean of precision and recall:

$$F_\beta = \frac{(1 + \beta^2) Precision \cdot Recall}{\beta^2 \cdot Precision + Recall}, \quad (4)$$

where β is the weight between *Precision* and *Recall*, and β^2 is often set to 0.3 to emphasize more on precision. Since different F-measure scores can be obtained according to different precision-recall pairs, in this paper, we report the maximum F-measure (F_β^{\max}) and mean F-measure (F_β^{mean}) computed from the PR curve. Besides, we also report the adaptive F-measure (F_β^{adp}) [73], whose threshold is computed as the twice of the mean of a saliency map.

Mean Absolute Error (M) [74] is defined as:

$$M = \frac{1}{N} \sum_{i=1}^N |S_i - G_i|, \quad (5)$$

where S_i and G_i denote the values at the i -th pixel in the saliency map and ground-truth map. N is the total number of pixels in the both map.

S-measure (S_α) [75], [76] was proposed to measure the spatial structure similarities between the saliency map and ground-truth. It is defined as:

$$S_\alpha = \alpha * S_o + (1 - \alpha) * S_r, \quad (6)$$

where S_o and S_r denote the object-aware and region-aware structural similarity, respectively, and α balances S_o and S_r . In this paper, we set $\alpha = 0.5$, as recommended in [75].

E-measure (E_ϕ) [77] is a recently proposed metric which considers both the local and global similarity between the prediction and ground-truth. It is defined as:

$$E_\phi = \frac{1}{w * h} \sum_{i=1}^w \sum_{j=1}^h \phi(i, j), \quad (7)$$

where $\phi(\cdot)$ denotes the enhanced alignment matrix [77]. w and h are the width and height of the ground-truth map, while (i, j) are pixel indexes. Since E_ϕ also performs a comparison between two binary maps, we treat it similarly to the F-measure, thresholding a saliency map with all possible values

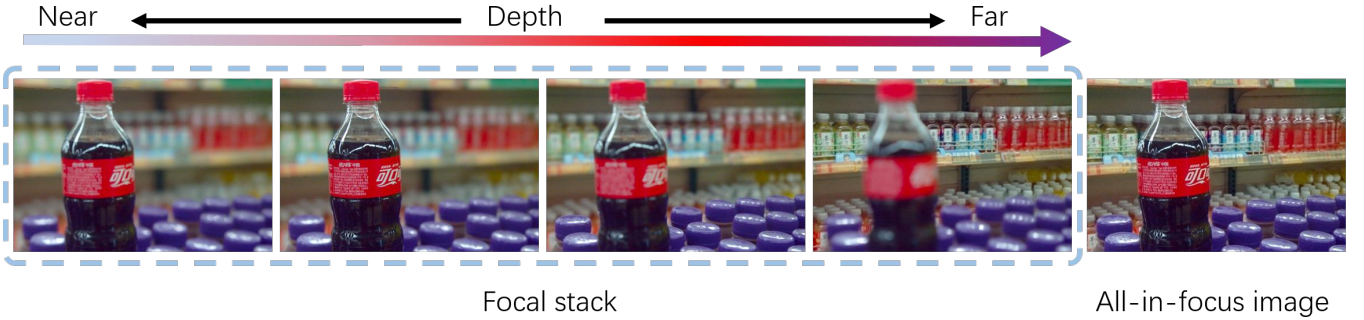


Fig. 10: Example of generated focal slices for Lytro Illum [52], together with the synthesized all-in-focus image.

and reporting the maximum and mean E_ϕ , denoted as E_ϕ^{\max} and E_ϕ^{mean} . Besides, adaptive E_ϕ , namely E_ϕ^{adp} , is computed similarly to the adaptive F-measure mentioned above, where the thresholds are two times the mean saliency values [73].

Note that, higher PR curves, F_β , S_α and E_ϕ , and lower M indicate better performance.

TABLE III: Dataset unification for light field SOD, which is in contrast to Table II. About the abbreviations: FS=focal stacks, DE=depth maps, MV=multi-view images, mL=Micro-lens images, Raw=raw light field data. Note that “○” indicates data that we have completed.

Datasets	FS	MV	DE	ML	Raw
LFSD [39]	✓	○	✓	○	✓
HFUT [44]	✓	✓	✓	○	
DUT-LF [49]	✓		✓		
DUT-MV [50]		✓			
Lytro Illum [52]	○	○	○	✓	✓

B. Dataset Unification

As shown in Section II-C and Table II, existing light field SOD datasets face the limitation of having non-unified data forms. This makes comprehensive benchmarking difficult. Since, due to the lack of specific data, some models cannot be correctly evaluated on certain datasets. To alleviate this issue, we generate supplemental data for existing datasets, making them more complete and unified. The completed data forms are illustrated in Table III, marked by “○”. Furthermore, we will release this data on our project site: <https://github.com/kerenfu/LFSOD-Survey> to facilitate future research in this field.

Generally, we can synthesize various data forms using the raw light field data, provided by two datasets, *i.e.*, LFSD and Lytro Illum. For Lytro Illum, we generate focal stacks (including all-in-focus images) and depth maps using the Lytro Desktop software. Regarding focal stack generation, we estimate the approximate focus range for each image scene, and then sample the focal slices within the focus range by an equal step. All-blurred or duplicated slices are removed. The final number of generated focal slices for Lytro Illum ranges from 2 to 16 for each scene, and about 74% of scenes have more than 6 slices. Fig. 10 shows an example of the generated focal stack. As mentioned in Section II-A2, multi-view images and micro-lens image arrays are generated by sampling the light field data in angular and spatial resolution,

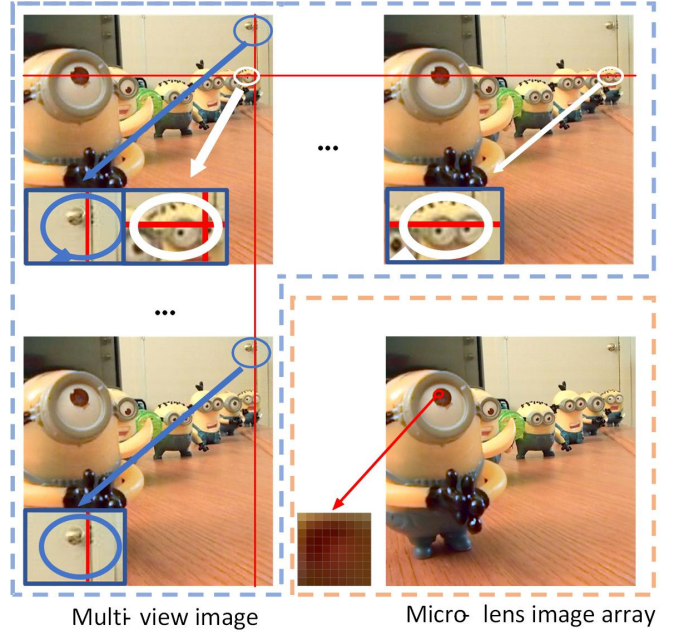


Fig. 11: Examples of generated multi-view images (360×360) and a micro-lens image array (1080×1080) for LFSD dataset [39]. As in Fig. 5, the bottom-left of each image shows zoomed-in details to better reflect the parallax. The micro-lens image array is composed of many micro-lens images [52].

respectively. Thus, these two data forms can be transformed between each other. In this way, we generate multi-view images for Lytro Illum from its micro-lens image arrays. We can also synthesize micro-lens image arrays for HFUT through the reverse operation. However, we cannot synthesize micro-lens image arrays for DUT-MV since the authors have only released the multi-view images in the vertical/horizontal direction. By using the raw data, we complement multi-view images and micro-lens image arrays for LFSD (Fig. 11). This complete data makes more comprehensive model evaluation possible. For example, models based on focal stacks, such as MoLF and ERNet, can now run and test on Lytro Illum. Note that for the remaining DUT-LF and DUT-MV, supplementing more data is possible in the future if the authors release the raw/more data. If this work has been done, DUT-LF/DUT-MV has the potential to be the *unified training dataset* for future models thanks to its large scale.

TABLE IV: Quantitative measures: S-measure (S_α) [75], max F-measure (F_β^{\max}), mean F-measure (F_β^{mean}) [73], adaptive F-measure (F_β^{adp}) [73], max E-measure (E_ϕ^{\max}), mean E-measure (E_ϕ^{mean}) [77], adaptive E-measure (E_ϕ^{adp}) [73] and MAE (M) [74] of seven light field SOD models (*i.e.*, LFS [39], WSC [40], DILF [25], DLSD [50], MoLF [26], ERNet [27], MAC [52]) and nine SOTA RGB-D based SOD models (*i.e.*, BBS [29], JLDLCF [28], SSF [32], UCNet [33], D3Net [34], S2MA [35], cmMS [36], HDFNet [37], and ATSA [30]). Note in the table, light field SOD models are marked by “†”. Symbol “N/T” indicates that a model was trained on quite some images from the corresponding dataset, and, thus, it is not tested. The top three models among light field and RGB-D based SOD models are highlighted in red, blue and green, separately. \uparrow/\downarrow denotes that a larger/smaller value is better.

	Traditional					Deep learning-based										
Metric	LFS [†] [39]	WSC [†] [40]	DILF [†] [25]	DLSD [†] [50]	MoLF [†] [26]	ERNet [†] [27]	MAC [†] [52]	BBS [29]	JLDCF [28]	SSF [32]	UCNet [33]	D3Net [34]	S2MA [35]	cmMS [36]	HDFNet [37]	ATSA [30]
LFSD [39]	$S_\alpha \uparrow$	0.681	0.700	0.811	0.786	0.835	0.832	0.782	0.864	0.862	0.859	0.858	0.825	0.837	0.850	0.858
	$F_\beta^{\max} \uparrow$	0.744	0.743	0.811	0.784	0.834	0.850	0.776	0.858	0.867	0.868	0.859	0.812	0.835	0.858	0.866
	$F_\beta^{\text{mean}} \uparrow$	0.513	0.722	0.719	0.758	0.809	0.836	0.733	0.842	0.848	0.862	0.848	0.796	0.806	0.850	0.818
	$F_\beta^{\text{adp}} \uparrow$	0.735	0.743	0.795	0.779	0.819	0.839	0.781	0.840	0.827	0.862	0.838	0.788	0.803	0.857	0.818
	$E_\phi^{\max} \uparrow$	0.809	0.787	0.861	0.859	0.888	0.886	0.832	0.900	0.902	0.901	0.898	0.863	0.873	0.896	0.902
	$E_\phi^{\text{mean}} \uparrow$	0.567	0.753	0.764	0.819	0.872	0.883	0.777	0.883	0.894	0.890	0.893	0.850	0.855	0.881	0.869
	$E_\phi^{\text{adp}} \uparrow$	0.773	0.788	0.846	0.852	0.886	0.887	0.837	0.889	0.882	0.896	0.890	0.853	0.863	0.890	0.872
	$M \downarrow$	0.205	0.151	0.136	0.117	0.089	0.082	0.127	0.072	0.070	0.067	0.072	0.095	0.094	0.073	0.068
HFUT [44]	$S_\alpha \uparrow$	0.565	0.613	0.675	0.711	0.742	0.778	0.731	0.751	0.789	0.725	0.748	0.785	0.729	0.723	0.763
	$F_\beta^{\max} \uparrow$	0.427	0.508	0.595	0.624	0.662	0.722	0.667	0.676	0.727	0.647	0.677	0.671	0.650	0.626	0.690
	$F_\beta^{\text{mean}} \uparrow$	0.323	0.493	0.513	0.594	0.639	0.709	0.620	0.654	0.707	0.639	0.672	0.651	0.623	0.617	0.669
	$F_\beta^{\text{adp}} \uparrow$	0.427	0.485	0.530	0.592	0.627	0.706	0.638	0.654	0.677	0.636	0.675	0.647	0.588	0.636	0.653
	$E_\phi^{\max} \uparrow$	0.637	0.695	0.750	0.784	0.812	0.841	0.797	0.801	0.844	0.816	0.804	0.797	0.777	0.784	0.801
	$E_\phi^{\text{mean}} \uparrow$	0.524	0.684	0.657	0.749	0.790	0.832	0.733	0.765	0.825	0.763	0.793	0.773	0.756	0.746	0.788
	$E_\phi^{\text{adp}} \uparrow$	0.666	0.680	0.693	0.755	0.785	0.831	0.772	0.804	0.811	0.781	0.810	0.789	0.744	0.779	0.789
	$M \downarrow$	0.221	0.154	0.144	0.111	0.094	0.082	0.107	0.089	0.075	0.090	0.090	0.091	0.112	0.097	0.095
Lytro Illum [52]	$S_\alpha \uparrow$	0.642	0.701	0.712	0.802	0.811	0.822	N/T	0.824	0.831	0.821	0.806	0.818	0.792	0.772	0.801
	$F_\beta^{\max} \uparrow$	0.529	0.639	0.607	0.753	0.794	0.817	N/T	0.769	0.813	0.776	0.761	0.773	0.739	0.700	0.748
	$F_\beta^{\text{mean}} \uparrow$	0.377	0.619	0.535	0.712	0.720	0.755	N/T	0.750	0.752	0.763	0.733	0.737	0.704	0.692	0.720
	$F_\beta^{\text{adp}} \uparrow$	0.528	0.610	0.592	0.709	0.695	0.746	N/T	0.749	0.734	0.763	0.727	0.723	0.698	0.720	0.722
	$E_\phi^{\max} \uparrow$	0.744	0.807	0.801	0.880	0.903	0.911	N/T	0.884	0.916	0.887	0.890	0.889	0.866	0.858	0.873
	$E_\phi^{\text{mean}} \uparrow$	0.553	0.794	0.704	0.839	0.865	0.884	N/T	0.870	0.883	0.881	0.872	0.870	0.844	0.814	0.856
	$E_\phi^{\text{adp}} \uparrow$	0.773	0.795	0.794	0.855	0.852	0.881	N/T	0.886	0.871	0.893	0.872	0.875	0.851	0.870	0.863
	$M \downarrow$	0.181	0.111	0.129	0.078	0.073	0.064	N/T	0.063	0.064	0.060	0.073	0.066	0.082	0.073	0.075
DUT-LF [49]	$S_\alpha \uparrow$	0.585	0.657	0.654	N/T	0.887	0.899	0.804	0.865	0.877	0.879	0.831	0.822	0.787	0.804	0.822
	$F_\beta^{\max} \uparrow$	0.533	0.621	0.585	N/T	0.903	0.908	0.792	0.852	0.878	0.887	0.816	0.797	0.754	0.803	0.801
	$F_\beta^{\text{mean}} \uparrow$	0.358	0.610	0.492	N/T	0.855	0.891	0.746	0.834	0.846	0.879	0.806	0.776	0.733	0.773	0.776
	$F_\beta^{\text{adapt}} \uparrow$	0.525	0.619	0.597	N/T	0.843	0.885	0.790	0.848	0.835	0.885	0.803	0.784	0.735	0.819	0.778
	$E_\phi^{\max} \uparrow$	0.711	0.789	0.757	N/T	0.939	0.949	0.863	0.900	0.925	0.922	0.876	0.860	0.839	0.879	0.864
	$E_\phi^{\text{mean}} \uparrow$	0.511	0.762	0.635	N/T	0.921	0.943	0.806	0.879	0.911	0.907	0.870	0.841	0.817	0.817	0.848
	$E_\phi^{\text{adapt}} \uparrow$	0.742	0.789	0.784	N/T	0.923	0.943	0.872	0.908	0.910	0.918	0.878	0.869	0.842	0.870	0.867
	$M \downarrow$	0.227	0.149	0.165	N/T	0.051	0.039	0.102	0.066	0.058	0.050	0.081	0.083	0.102	0.079	0.091

C. Performance Benchmarking and Analysis

To provided in-depth understanding of the performance of different models, we conduct the first comprehensive benchmarking of seven light field SOD models (*i.e.*, LFS [39], WSC [40], DILF [25], DLSD [50], MoLF [26], ERNet [27], MAC [52]) and nine SOTA RGB-D based SOD models⁸ (*i.e.*, BBS [29], JLDLCF [28], SSF [32], UCNet [33], D3Net [34], S2MA [35], cmMS [36], HDFNet [37], and ATSA [30]) on four existing light field datasets, including the entire LFSD (100 light fields), HFUT (255 light fields), Lytro Illum (640

light fields) datasets and the test set (462 light fields) of DUT-LF. Sample images from these datasets are shown in Fig. 7. All the benchmarked models have either publicly available source/executable codes or results provided by the authors. The eight evaluation metrics described previously (*i.e.*, PR, S-measure, max/mean F-measure, max/mean E-measure, adaptive F-measure and E-measure, mean absolute error) are adopted and the results are reported in Table IV. Meanwhile, the PR curves, max F-measure curves and visual comparisons are shown in Fig. 12, Fig. 13, Fig. 14 and Fig. 15. It is worth noting that the evaluation is not conducted on the DUT-MV dataset [50] since it only provides multi-view images, which are not compatible with the input data forms of other light field SOD models. Further, note that DLSD [50] is not tested on the DUT-LF test set because it used quite some test images ($\sim 36\%$, according to our verification) from this dataset for training. Also, MAC is not evaluated on Lytro

⁸The RGB-D SOD models benchmarked in this paper are selected according to the top models concluded by the recent survey [63] and also the latest open-source models published in ECCV-2020. All depth maps fed to a model are unnormalized (using their original values) and are optionally reversed on an entire dataset to fit the best performance of this model. All RGB-D SOD models are not re-trained in our experiments, and instead just use their released model weights trained on RGB-D data. This generally evaluates how well they can generalize to the light field images.

Illum since the authors conducted five-fold cross-validation on this dataset, and therefore it is not directly comparable to other models. In addition, for ERNet [27], we only evaluate the teacher model since its pre-trained student model is not publicly available. Analyses based on Table IV and Fig. 12 are given as followings.

1) *Traditional vs. Deep Light Field SOD Models:* Compared to the three traditional models shown in Table I, the deep learning-based SOD models clearly have a significant performance boost on all datasets. This confirms the power of deep neural networks when applied to this field.

2) *Deep Learning-Based Light Field SOD Models:* As shown in Table I, MoLF and ERNet adopt focal stacks and all-in-focus images as input data forms, while DLSD and MAC use center-view images and micro-lens image arrays. From Table IV and Fig. 12, it is clear that MoLF and ERNet outperform DLSD and MAC. It is also worth noting that MoLF and ERNet achieve the two best performances, which is probably because that the two models were trained on the large-scale DUT-LF dataset (*i.e.*, 1,000 light fields). Besides, the results indicate that models based on multi-view or micro-lens images are not as effective as those based on focal stacks. This is probably because that the former are less studied, and the effectiveness of multi-view and micro-lens images is still underexplored. Moreover, the training data may also matter because MAC was trained only on Lytro Illum, which is about twice smaller than DUT-LF. Among the above four models compared, ERNet attains the best accuracy.

3) *Comparison Between Light Field SOD and RGB-D SOD Models:* From the quantitative results illustrated in Table IV and Fig. 12, it can be observed that, the latest cutting-edge RGB-D models achieve comparable or even better performance than the light field SOD models. Three RGB-D models, namely JLDCE, SSF, and ATSA, achieve generally better performance than ERNet on LFSD, HFUT and Lytro Illum. The underlying reasons of the superiority of RGB-D based SOD models may be two-fold. First, RGB-D based SOD has recently drawn extensive research interest and many elaborate models have been proposed. Inspired by previous research on the RGB SOD problem [78]–[80], these models often pursue edge-preserving results from deep neural networks and employ functional modules/architectures, such as a boundary supplement unit [32], multi-scale feature aggregation module [30], or UNet-shaped bottom-up/top-down architecture [28], [35], [81] to achieve this goal. In contrast, light field SOD has been less explored and the models/architectures have evolved slowly. Edge-aware properties have not yet been considered by most existing models. Besides, although the attention mechanism and ConvLSTM are adopted in ERNet, no top-down refinement is implemented to generate a saliency map with more accurate boundaries. As evidenced in Fig. 1 and Fig. 14, the RGB-D SOD models tend to detect more accurate boundaries than existing deep light field SOD models. The other potential reason could be that the RGB-D SOD models are trained on more data. For instance, JLDCE was trained on 2,200 RGB-D scenarios according to [28], while ERNet [27] was trained only on $\sim 1,000$ light fields. Thus, the former is more likely to obtain better generalizability.

However, although RGB-D models only leverage depth information, which is a subset information of light fields, we can still hardly deny the potentials of light fields on boosting the performance of SOD, as recently RGB-D SOD area is much more active (many new competitive models are proposed as mentioned in [63]) than the area of light field SOD. Besides, the performance of ERNet and MoLF is only slightly lower than that of the RGB-D models on the three datasets, which further validates the effectiveness of light fields for SOD [54]. We conclude that there is still considerable room for improving light field SOD, because light fields can provide much more information than a pair of RGB and depth images.

4) *Accuracy Across Different Aatasets:* It is clearly shown in Table IV and Fig. 12 that the models tested perform differently on different datasets. Generally, the models achieve better results on LFSD than on the other three datasets, indicating that LFSD is the easiest dataset for light field SOD, on which the traditional model DILF can even outperform some deep models like DLSD and MAC. In contrast, HFUT, Lytro Illum and DUT-LF are more challenging. From Fig. 7, it is also clear that, with the exception of LFSD, the datasets have limited light field depth ranges. Note that MoLF, ERNet, ATSA behave prominently on DUT-LF, probably because they were trained on DUT-LF's training set or training data (Table I). Besides, as mentioned in Section II-C, HFUT has many small salient objects, with multiple objects existed per image. The degraded performance of these models on this dataset tells that detecting small/multiple salient objects is still very challenging for existing techniques, no matter for both RGB-D based models or light field models. This makes HFUT the most difficult among the existing light field datasets.

5) *Results Visualization:* Fig. 14 visualizes some sample results from five light field models, including two traditional methods (*i.e.*, LFS and DILF) and three deep learning-based models (*i.e.*, DLSD, MoLF and ERNet), and three latest RGB-D based models (*i.e.*, JLDCE, BBS, and ATSA). The first two rows in Fig. 14 show easy cases while the third to fifth rows show cases with complex backgrounds or sophisticated boundaries. The last row gives an example with low color contrast between foreground and background. As can be observed from Fig. 14, RGB-D models perform comparably to or even better than light field models, which confirms the fact that this field is still insufficiently studied. Fig. 15 further shows several scenarios with small and multiple salient objects, where the first three rows show the cases with multiple salient objects and the others show the cases of small objects. According to Fig. 15, both RGB-D based and light field models are more likely to result in erroneous detection, confirming the challenge of handling small/multiple objects for existing techniques.

IV. CHALLENGES AND OPEN DIRECTIONS

This section highlights several future research directions for light field SOD and outlines several open issues.

A. Dataset Collection and Unification

As demonstrated in Section II-C, existing light field datasets are limited in scale and have non-unified data forms, making

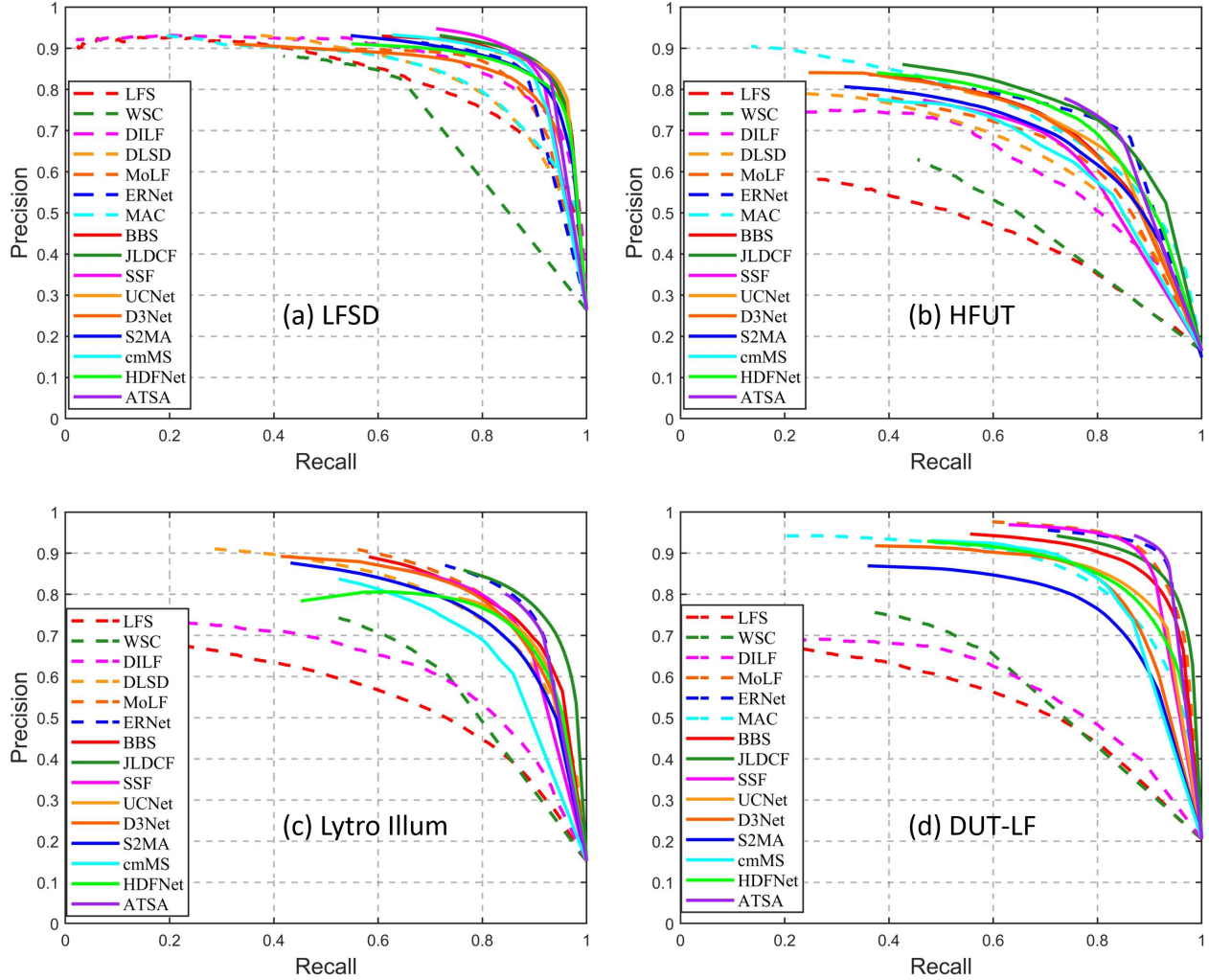


Fig. 12: PR curves on four datasets ((a) LFSD [39], (b) HFUT [44], (c) Lytro Illum [52], and (d) DUT-LF [49]) for seven light field SOD models (*i.e.*, LFS [39], WSC [40], DILF [25], DLSD [50], MoLF [26], ERNet [27], MAC [52]) and nine SOTA RGB-D based SOD models (*i.e.*, BBS [29], JLDCF [28], SSF [32], UCNet [33], D3Net [34], S2MA [35], cmMS [36], HDFNet [37], and ATSA [30]). Note that in this figure, the *solid lines* and *dashed lines* represent the PR curves of *RGB-D based SOD models* and *light field SOD models*, respectively.

it difficult to evaluate different models and generalize deep networks. This data issue is *particularly severe* for light field SOD because of its diverse data representations and high dependency on special acquisition hardware, differing it from other SOD tasks (*e.g.*, RGB-D SOD [28], [30], [32], video SOD [82], [83]) in the saliency community. Therefore, developing large-scale and unified datasets is essential for future research. We urge researchers to take this issue into consideration when constructing new datasets. Providing complete data forms including raw data, focal stacks, multi-view images, depth maps, and micro-lens image arrays would definitely facilitate and advance research on this topic. However, we also note there is a challenge in data storage and transmission, since raw light field data is quite large in size (*e.g.*, the 640 light fields of Lytro Illum occupy 32.8 Gigabytes), not to say together with other data forms of a large-scale dataset, making the entire dataset a bit difficult to spread. Anyway, it will still

be great if a subset of any data form is available for public.

B. Further Investigation Needed in Light Field SOD

As discussed, there are currently fewer studies regarding SOD on light fields compared to other areas in the saliency community. Thus, this field is still less active and under-explored. Further, from the benchmarking results in Section III-C, we can conclude that the SOTA performance is still far from satisfactory, especially on the HFUT dataset. Considerable room exists for further improvement on algorithms/models. Also note that only seven models using modern deep learning techniques emerged between 2019 and 2020. We attribute such scarce research on light field SOD to the data issue mentioned previously, as well as the lack of a complete survey of existing methods and datasets on this topic, which is rightly the goal of this paper.

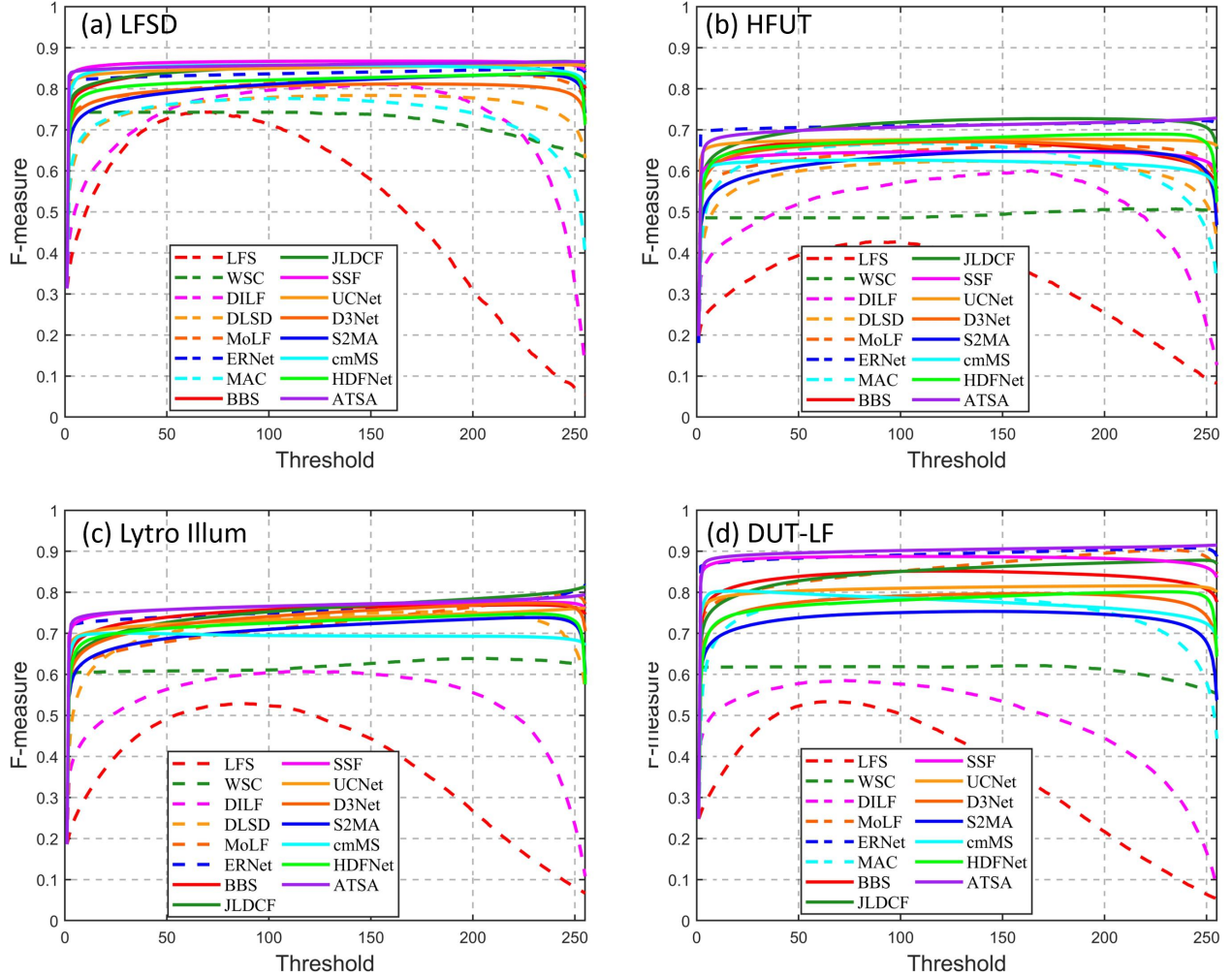


Fig. 13: F-measure curves under different thresholds on four datasets ((a) LFSD [39], (b) HFUT [44], (c) Lytro Illum [52] and (d) DUT-LF [49]) for seven light field SOD models (*i.e.*, LFS [39], WSC [40], DILF [25], DLSD [50], MoLF [26], ERNet [27], MAC [52]) and nine SOTA RGB-D based SOD models (*i.e.*, BBS [29], JLDCE [28], SSF [32], UCNet [33], D3Net [34], S2MA [35], cmMS [36], HDFNet [37], and ATSA [30]). Note that in this figure, the *solid lines* and *dashed lines* represent the F-measure curves of *RGB-D based SOD models* and *light field SOD models*, respectively.

C. Multi-view Images and Micro-lens Image Arrays

Most existing models work with focal stacks and depth maps, as surveyed in Table I, while multi-view images and micro-lens image arrays are two other types of light field data representations which are seldom considered (only five related models). The benchmarking results in Section III-C imply that the related models do not perform as well as models utilizing other data forms, so the utilization of these two data forms is still insufficiently explored. More new models are expected in the future to explore the effectiveness of multi-view images and micro-lens image arrays for light field SOD. Another potential reason could be that, these two data forms themselves may be less information-representative than focal stacks and depth maps, namely scene depth information is conveyed more implicitly. This could make finding effective mappings and mining underlying rules using deep neural networks difficult, especially when the training data is sparse. In addition, the

comparison between different data forms on the effectiveness and redundancy for saliency detection is an interesting work.

D. Incorporating High-Quality Depth Estimation

It has been proven that accurate depth maps are conducive to discovering salient objects from complex backgrounds. Unfortunately, the quality of depth maps currently provided varies greatly, since depth estimation from light fields is a challenging problem [56]–[59], easily leading to imperfect depth. The challenge arises from the fact that, although the light fields can be used to synthesize images focused at any depth through digital refocusing techniques, the depth assignment of each scene point is unknown and resorts to the judgement of whether an image region is in-focus, which itself is an open problem [84], [85]. Imperfect depth maps often result in a negative effect on detection accuracy for models using depth maps. Therefore, incorporating high-quality depth

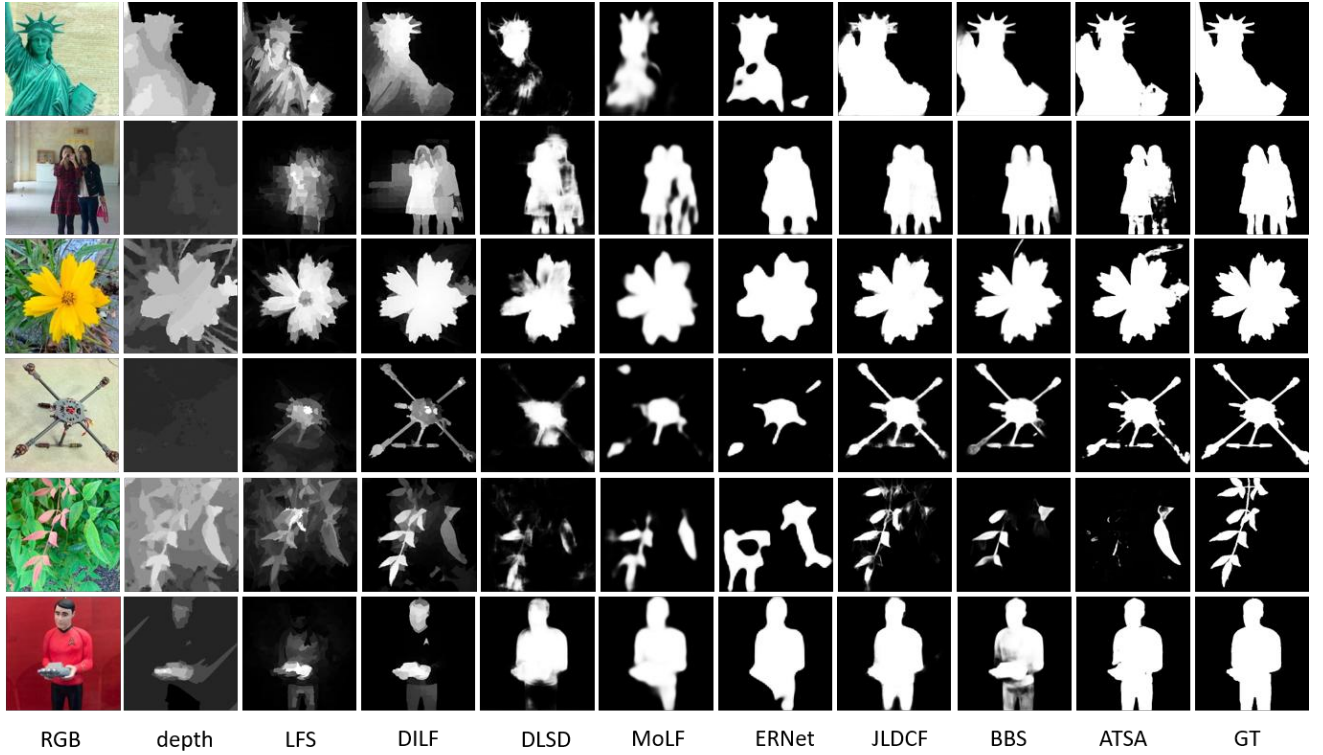


Fig. 14: Visual comparison of five light field SOD (*i.e.*, LFS [39], DILF [25], DLSD [50], MoLF [26] and ERNet [27]) and three SOTA RGB-D based SOD models (*i.e.*, JLDCF [28], BBS [29], and ATSA [30]).

estimation algorithms from light field is for sure beneficial for boosting performance.

E. Edge-Aware Light Field SOD

Accurate object boundaries are essential for high-quality saliency maps, as SOD is a pixel-wise segmentation task [4]. In the RGB SOD field, edge-aware SOD models are drawing increasing research attention [78]–[80]. Currently, as shown through our experimental results, existing deep light field SOD models seldom consider this issue and obtain saliency results with coarse boundaries/edges, implying that edge-aware light field SOD could be a future direction for research.

F. Development of Acquisition Technology and Hardware

As we mentioned before, the first generation light field camera, named Lytro, was invented in 2011, while its successor, called Lytro Illum, was introduced in 2014. The latter is more powerful but has a much large size than the former and is also much more expensive. However, generally speaking, the development of acquisition technology and hardware of light field is slow compared to other IT areas such as computers and mobile phones, with very few commercial light field cameras introduced since 2014. Therefore technological developments on acquisition and hardware are urgently required for light field photography. Currently, in terms of image quality, as well as price and portability, light field cameras are still far from replacing conventional RGB cameras. Imagining that in the future if the light field cameras become affordable and

small in size, which can easily be integrated into our mobile phones, everyone can try light field photography in our daily life. This would provide a vast increase in user data and post-processing application requirements, paving the way for significant improvements in light field SOD.

G. Linking RGB-D SOD to Light Field SOD

There is a close connection between light field SOD and RGB-D SOD, since both tasks often explore scene depth information for saliency detection, whereas depth information can be derived from light field data via different techniques. That is why RGB-D SOD could be deemed as a degenerated solution for tackling light field SOD. As shown in Table IV, applying RGB-D SOD models to light field is straightforward, whereas we believe its reverse could also be possible. For example, intuitively, reconstructing light field data such as focal stacks or multi-view images from a pair of RGB and depth images is possible (*e.g.*, [50]). If this bridge is achieved, mutual transfer between the models of these two fields becomes feasible, and light field models can then be applied to RGB-D data. Such a link would be an interesting issue to explore in the near future.

H. Different Supervision Strategies

Existing deep light field models learn to segment salient objects in a fully supervised manner, which demands sufficient annotated training data. Unfortunately, as mentioned before, existing datasets are limited in scale, *e.g.*, DUT-LF and DUT-MV provide 1,000 and 1,100 samples for training, respectively,

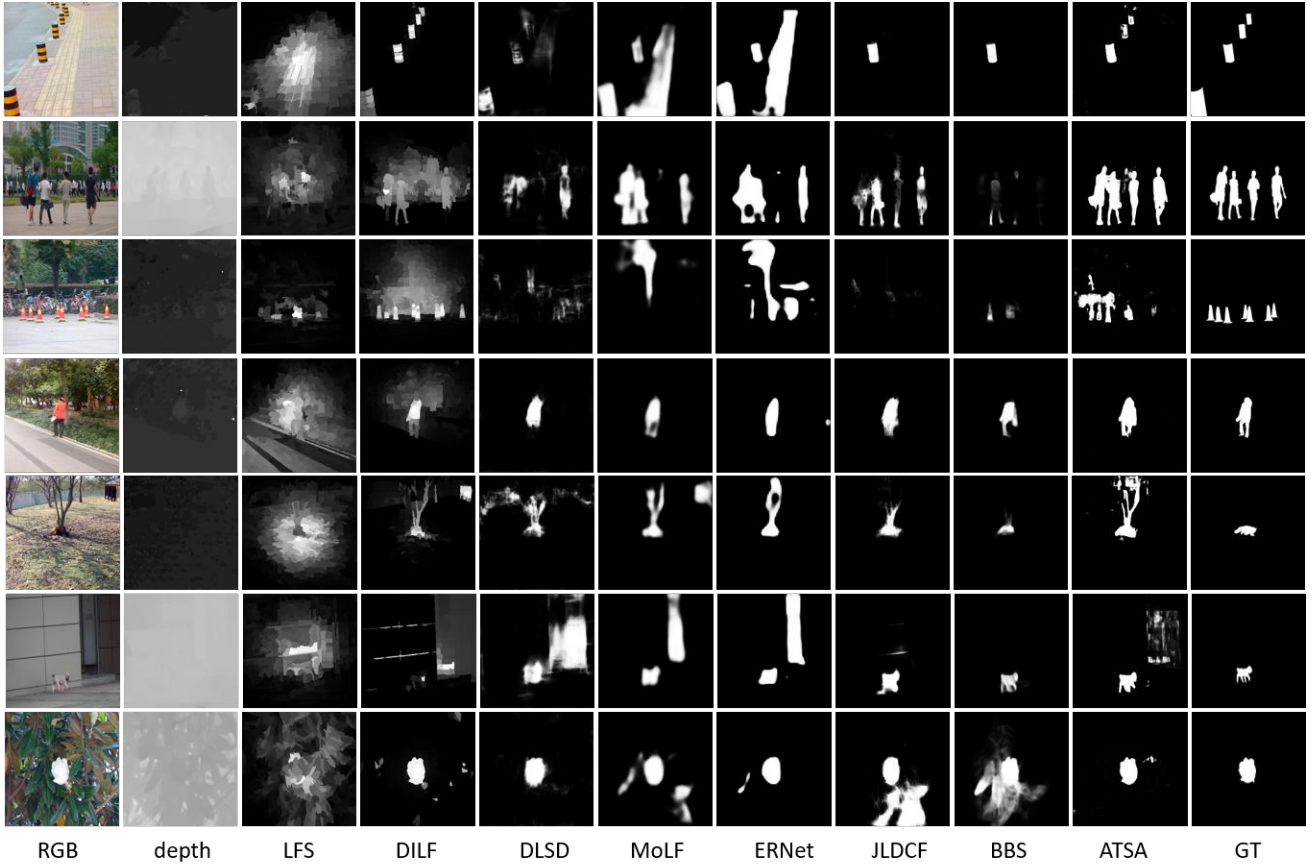


Fig. 15: Visual comparison of five light field SOD (*i.e.*, LFS [39], DILF [25], DLSD [50], MoLF [26] and ERNet [27]) and three SOTA RGB-D based SOD models (*i.e.*, JLDCF [28], BBS [29], and ATSA [30]) on detecting small and multiple objects.

while other datasets contain fewer than 640 light fields. On one hand, a small amount training data limits the generalization ability of models. On the other hand, acquiring a large amount of annotated data requires extreme manual effort on data collection and labeling. Recently, weakly and semi-supervised learning strategies have drawn extensive research attention, largely reducing the annotation effort. Because of being data-friendly, they have been introduced to RGB SOD and some encouraging attempts [8], [86], [87] have been made. Inspired by this, one future direction is to extend these supervision strategies to light field SOD to overcome the shortage of training data. Additionally, several works [88], [89] have proven that pre-training models in a self-supervised manner can effectively improve the performance, which can also be introduced to light field SOD in the future.

I. Other Potential Directions

There are several other potential directions for future research inspired by the recent advances in the saliency community. For example, high-resolution salient object detection [90] aims to handle salient object segmentation in high-resolution images, thus achieving high-resolution details could be considered in light field SOD. Besides, while existing light field datasets are labeled at an object-level, instance-level annotation and detection, which aim at separating individual objects [91]–[94], could also be introduced into this field. Note

that there are quite some instance-sensitive application scenarios, *e.g.*, image captioning [95], and multi-label image recognition [96], as well as various weakly supervised/unsupervised learning scenarios [97], [98]. One recent work attempted to address weakly-supervised salient instance detection [99]. Similarly, more effort could be spent on instance-level ground-truth annotation and designing instance-level light field SOD models. Furthermore, as we know, eye-fixation prediction [3]–[5] is another subfield of saliency detection. Till now no research has been conducted on eye-fixation prediction using light field data. As abundant natural scene information is provided by light field, we hope that the various data forms of light field, which provide useful cues, can help eliminate ambiguous eye-fixation. Lastly, light field data could benefit other closely related tasks to SOD, such as camouflaged object detection (COD) [100] and transparent object segmentation [101], where objects often borrow texture from their background and have similar appearances to their surroundings.

Finally, there is an unanswered question remaining: *how can light field information benefit SOD over depth information?* As we know, depth information can be derived from and is a subset of light field data. Different forms of light field data, *e.g.*, focal stacks and multi-view images, somewhat imply depth information, indicating that existing models may leverage such depth information in an implicit way. So how is the gap between using depth in an explicit way (like RGB-

D SOD models do) and in an implicit way? This is an interesting question, but unfortunately, since the problem of light field SOD was proposed in 2014, no any study showed any direct answer/evidence. Such an answer deserves further investigation and understanding into this field in the future.

V. CONCLUSION

We have provided the first comprehensive review and benchmark for light field SOD, reviewing and discussing existing studies and related datasets. We have benchmarked representative light field SOD models and compared them to several cutting-edge RGB-D SOD models both qualitatively and quantitatively. Considering the fact that the existing light field datasets are somewhat inconsistent in data forms, we generated supplemental data for existing datasets, making them more complete and unified. Moreover, we have discussed several potential directions for future research and outlined some open issues. Although progress has been made over the past several years, there are still only seven deep learning-based works focusing on this topic, leaving significant room for designing more powerful network architectures and incorporating effective modules (e.g., edge-aware designs and top-down refinement) for improving SOD performance. We hope this survey will serve as a catalyst to advance this area and promote interesting works in the future.

REFERENCES

- [1] M.-M. Cheng, G.-X. Zhang, N. Mitra, X. Huang, and S. Hu, "Global contrast based salient region detection," in *Proceedings of the IEEE Conference on Computer Vision and Pattern Recognition*, 2011, pp. 409–416.
- [2] A. Borji, D. N. Sihite, and L. Itti, "Quantitative analysis of human-model agreement in visual saliency modeling: A comparative study," *IEEE Transactions on Image Processing*, vol. 22, pp. 55–69, 2013.
- [3] A. Borji, "Saliency prediction in the deep learning era: Successes and limitations," *IEEE Transactions on Pattern Analysis and Machine Intelligence*, 2019.
- [4] A. Borji, M. Cheng, H. Jiang, and J. Li, "Salient object detection: A benchmark," *IEEE Transactions on Image Processing*, vol. 24, pp. 5706–5722, 2015.
- [5] A. Borji and L. Itti, "State-of-the-art in visual attention modeling," *IEEE Transactions on Pattern Analysis and Machine Intelligence*, vol. 35, pp. 185–207, 2013.
- [6] G. Liu and D. Fan, "A model of visual attention for natural image retrieval," in *Proceedings of the IEEE Conference on Information Science and Cloud Computing Companion*. IEEE, 2013, pp. 728–733.
- [7] Z. Ren, S. Gao, L. Chia, and I. Tsang, "Region-based saliency detection and its application in object recognition," *IEEE Transactions on Circuits and Systems for Video Technology*, vol. 24, pp. 769–779, 2014.
- [8] D. Zhang, D. Meng, L. Zhao, and J. Han, "Bridging saliency detection to weakly supervised object detection based on self-paced curriculum learning," in *Proceedings of the International Joint Conferences on Artificial Intelligence*, 2016.
- [9] U. Rutishauser, D. B. Walther, C. Koch, and P. Perona, "Is bottom-up attention useful for object recognition?" in *Proceedings of the IEEE Conference on Computer Vision and Pattern Recognition*, 2004.
- [10] F. Moosmann, D. Larlus, and F. Jurie, "Learning saliency maps for object categorization," in *Eccv International Workshop on the Representation & Use of Prior Knowledge in Vision*, 2006.
- [11] Y. Wei, J. Feng, X. Liang, M.-M. Cheng, Y. Zhao, and S. Yan, "Object region mining with adversarial erasing: A simple classification to semantic segmentation approach," in *Proceedings of the IEEE Conference on Computer Vision and Pattern Recognition*, 2017, pp. 6488–6496.
- [12] Y. Wei, X. Liang, Y. Chen, X. Shen, M.-M. Cheng, Y. Zhao, and S. Yan, "Stc: A simple to complex framework for weakly-supervised semantic segmentation," *IEEE Transactions on Pattern Analysis and Machine Intelligence*, vol. 39, pp. 2314–2320, 2017.
- [13] X. Wang, S. You, X. Li, and H. Ma, "Weakly-supervised semantic segmentation by iteratively mining common object features," in *Proceedings of the IEEE Conference on Computer Vision and Pattern Recognition*, 2018, pp. 1354–1362.
- [14] W. Wang, J. Shen, R. Yang, and F. Porikli, "Saliency-aware video object segmentation," *IEEE Transactions on Pattern Analysis and Machine Intelligence*, vol. 40, pp. 20–33, 2018.
- [15] H. Song, W. Wang, S. Zhao, J. Shen, and K. Lam, "Pyramid dilated deeper convlstm for video salient object detection," in *Proceedings of the European Conference on Computer Vision*, 2018.
- [16] J. Han, E. J. Pauwels, and P. M. de Zeeuw, "Fast saliency-aware multi-modality image fusion," *Neurocomputing*, vol. 111, pp. 70–80, 2013.
- [17] W. Wang, J. Shen, and H. Ling, "A deep network solution for attention and aesthetics aware photo cropping," *IEEE Transactions on Pattern Analysis and Machine Intelligence*, vol. 41, pp. 1531–1544, 2019.
- [18] J. Sun and H. Ling, "Scale and object aware image retargeting for thumbnail browsing," in *Proceedings of the IEEE International Conference on Computer Vision*, 2011, pp. 1511–1518.
- [19] Y.-F. Ma, L. Lu, H. Zhang, and M. Li, "A user attention model for video summarization," in *MULTIMEDIA '02*, 2002.
- [20] D. Simakov, Y. Caspi, E. Shechtman, and M. Irani, "Summarizing visual data using bidirectional similarity," *Proceedings of the IEEE Conference on Computer Vision and Pattern Recognition*, pp. 1–8, 2008.
- [21] Y. Sugano, Y. Matsushita, and Y. Sato, "Calibration-free gaze sensing using saliency maps," in *Proceedings of the IEEE Conference on Computer Vision and Pattern Recognition*, 2010, pp. 2667–2674.
- [22] A. Borji and L. Itti, "Defending yarbush: eye movements reveal observers' task," *Journal of vision*, vol. 14 3, p. 29, 2014.
- [23] A. Karpathy, S. Miller, and L. Fei-Fei, "Object discovery in 3d scenes via shape analysis," *2013 IEEE International Conference on Robotics and Automation*, pp. 2088–2095, 2013.
- [24] S. Frintrop, G. M. García, and A. B. Cremers, "A cognitive approach for object discovery," *2014 22nd International Conference on Pattern Recognition*, pp. 2329–2334, 2014.
- [25] J. Zhang, M. Wang, J. Gao, Y. Wang, X. Zhang, and X. Wu, "Saliency detection with a deeper investigation of light field," in *Proceedings of the International Joint Conferences on Artificial Intelligence*, 2015.
- [26] M. Zhang, J. Li, J. Wei, Y. Piao, and H. Lu, "Memory-oriented decoder for light field salient object detection," in *Proceedings of the Advances in Neural Information Processing Systems*, 2019.
- [27] Y. Piao, Z. Rong, M. Zhang, and H. Lu, "Exploit and replace: An asymmetrical two-stream architecture for versatile light field saliency detection," in *AAAI*, 2020.
- [28] K. Fu, D.-P. Fan, G.-P. Ji, and Q. Zhao, "Jl-dcf: Joint learning and densely-cooperative fusion framework for rgb-d salient object detection," in *Proceedings of the IEEE Conference on Computer Vision and Pattern Recognition*, 2020, pp. 3049–3059.
- [29] D.-P. Fan, Y. Zhai, A. Borji, J. Yang, and L. Shao, "Bbs-net: Rgb-d salient object detection with a bifurcated backbone strategy network," in *Proceedings of the European Conference on Computer Vision*, vol. abs/2007.02713, 2020.
- [30] M. Zhang, S. X. Fei, J. Liu, S. Xu, Y. Piao, and H. Lu, "Asymmetric two-stream architecture for accurate rgb-d saliency detection," in *Proceedings of the European Conference on Computer Vision*, 2020.
- [31] D.-P. Fan, M.-M. Cheng, J.-J. Liu, S.-H. Gao, Q. Hou, and A. Borji, "Salient objects in clutter: Bringing salient object detection to the foreground," in *Proceedings of the Conference on European conference on computer vision*, 2018, pp. 186–202.
- [32] M. Zhang, W. Ren, Y. Piao, Z. Rong, and H. Lu, "Select, supplement and focus for rgb-d saliency detection," in *Proceedings of the IEEE Conference on Computer Vision and Pattern Recognition*, 2020, pp. 3469–3478.
- [33] J. Zhang, D.-P. Fan, Y. Dai, S. Anwar, F. S. Saleh, T. Zhang, and N. Barnes, "Uc-net: Uncertainty inspired rgb-d saliency detection via conditional variational autoencoders," in *Proceedings of the IEEE Conference on Computer Vision and Pattern Recognition*, 2020, pp. 8579–8588.
- [34] D.-P. Fan, Z. Lin, J. Zhao, Y. Liu, Z. Zhang, Q. Hou, M. Zhu, and M.-M. Cheng, "Rethinking rgb-d salient object detection: Models, datasets, and large-scale benchmarks," *IEEE Transactions on Neural Networks and Learning Systems*, vol. PP, 2020.

- [35] N. Liu, N. Zhang, and J. Han, "Learning selective self-mutual attention for rgb-d saliency detection," in *Proceedings of the IEEE Conference on Computer Vision and Pattern Recognition*, 2020, pp. 13 753–13 762.
- [36] C. Li, R. Cong, Y. Piao, Q. Xu, and C. C. Loy, "Rgb-d salient object detection with cross-modality modulation and selection," in *Proceedings of the European Conference on Computer Vision*, vol. abs/2007.07051, 2020.
- [37] Y. Pang, L. Zhang, X.-Q. Zhao, and H. Lu, "Hierarchical dynamic filtering network for rgb-d salient object detection," in *Proceedings of the European Conference on Computer Vision*, vol. abs/2007.06227, 2020.
- [38] H.-F. Li, G. Chen, G. Li, and Y. Yu, "Motion guided attention for video salient object detection," in *Proceedings of the IEEE International Conference on Computer Vision*, 2019, pp. 7273–7282.
- [39] N. Li, J. Ye, Y. Ji, H. Ling, and J. Yu, "Saliency detection on light field," in *Proceedings of the IEEE Conference on Computer Vision and Pattern Recognition*, 2014, pp. 2806–2813.
- [40] N. Li, B. Sun, and J. Yu, "A weighted sparse coding framework for saliency detection," in *Proceedings of the IEEE Conference on Computer Vision and Pattern Recognition*, 2015, pp. 5216–5223.
- [41] H. Sheng, S. Zhang, X. Liu, and Z. Xiong, "Relative location for light field saliency detection," in *Proceedings of the IEEE International Conference on Acoustics, Speech and Signal Processing*, 2016, pp. 1631–1635.
- [42] A. Wang, M. Wang, X. Li, Z. Mi, and H. Zhou, "A two-stage bayesian integration framework for salient object detection on light field," *Neural Processing Letters*, vol. 46, pp. 1083–1094, 2017.
- [43] N. Li, J. Ye, Y. Ji, H. Ling, and J. Yu, "Saliency detection on light field," *IEEE Transactions on Pattern Analysis and Machine Intelligence*, vol. 39, no. 8, pp. 1605–1616, 2017.
- [44] J. Zhang, M. Wang, L. Lin, X. Yang, J. Gao, and Y. Rui, "Saliency detection on light field: A multi-cue approach," *ACM Transactions on Multimedia Computing, Communications, and Applications (TOMM)*, vol. 13, no. 3, pp. 1–22, 2017.
- [45] H. Wang, B. Yan, X. Wang, Y. Zhang, and Y. Yang, "Accurate saliency detection based on depth feature of 3d images," *Multimedia Tools and Applications*, vol. 77, no. 12, pp. 14 655–14 672, 2018.
- [46] S. Wang, W. Liao, P. Surman, Z. Tu, Y. Zheng, and J. Yuan, "Salience guided depth calibration for perceptually optimized compressive light field 3d display," in *Proceedings of the IEEE Conference on Computer Vision and Pattern Recognition*, 2018, pp. 2031–2040.
- [47] X. Wang, Y. Dong, Q. Zhang, and Q. Wang, "Region-based depth feature descriptor for saliency detection on light field," *Multimedia Tools and Applications*, pp. 1–18, 2020.
- [48] Y. Piao, X. Li, M. Zhang, J. Yu, and H. Lu, "Saliency detection via depth-induced cellular automata on light field," *IEEE Transactions on Image Processing*, vol. 29, pp. 1879–1889, 2020.
- [49] T. Wang, Y. Piao, H. Lu, X. chun Li, and L. Zhang, "Deep learning for light field saliency detection," in *Proceedings of the IEEE International Conference on Computer Vision*, 2019, pp. 8837–8847.
- [50] Y. Piao, Z. Rong, M. Zhang, X. Li, and H. Lu, "Deep light-field-driven saliency detection from a single view," in *Proceedings of the International Joint Conferences on Artificial Intelligence*, 2019.
- [51] M. Zhang, W. Ji, Y. Piao, J. Li, Y. Zhang, S. Xu, and H. Lu, "Lfnet: Light field fusion network for salient object detection," *IEEE Transactions on Image Processing*, vol. 29, pp. 6276–6287, 2020.
- [52] J. Zhang, Y. Liu, S. Zhang, R. Poppe, and M. Wang, "Light field saliency detection with deep convolutional networks," *IEEE Transactions on Image Processing*, vol. 29, pp. 4421–4434, 2020.
- [53] Q. Zhang, S. Wang, X. Wang, Z. Sun, S. Kwong, and J. Jiang, "A multi-task collaborative network for light field salient object detection," *IEEE Transactions on Circuits and Systems for Video Technology*, 2020.
- [54] X. Zhang, Y. Wang, J. Zhang, L. Hu, and M. Wang, "Light field saliency vs. 2d saliency: A comparative study," *Neurocomputing*, vol. 166, pp. 389–396, 2015.
- [55] A. Gershun, "The light field," *Studies in Applied Mathematics*, vol. 18, no. 1–4, p. 51–151, 1939.
- [56] H. Jeon, J. Park, G. Choe, J. Park, Y. Bok, Y.-W. Tai, and I.-S. Kweon, "Accurate depth map estimation from a lenslet light field camera," in *Proceedings of the IEEE Conference on Computer Vision and Pattern Recognition*, 2015, pp. 1547–1555.
- [57] M. W. Tao, S. Hadap, J. Malik, and R. Ramamoorthi, "Depth from combining defocus and correspondence using light-field cameras," in *Proceedings of the IEEE International Conference on Computer Vision*, 2013, pp. 673–680.
- [58] M. W. Tao, P. P. Srinivasan, J. Malik, S. Rusinkiewicz, and R. Ramamoorthi, "Depth from shading, defocus, and correspondence using light-field angular coherence," in *Proceedings of the IEEE Conference on Computer Vision and Pattern Recognition*, 2015, pp. 1940–1948.
- [59] T. Wang, A. A. Efros, and R. Ramamoorthi, "Occlusion-aware depth estimation using light-field cameras," in *Proceedings of the IEEE International Conference on Computer Vision*, 2015, pp. 3487–3495.
- [60] R. Ng, M. Levoy, M. Brédif, G. Duval, M. Horowitz, and P. Hanrahan, "Light field photography with a hand-held plenoptic camera," *Technical Report CTSR 2005-02*, vol. CTSR, 01 2005.
- [61] P. Jiang, H. Ling, J. Yu, and J. Peng, "Salient region detection by ufo: Uniqueness, focusness and objectness," in *Proceedings of the IEEE International Conference on Computer Vision*, 2013, pp. 1976–1983.
- [62] C. Buehler, M. Bosse, L. McMillan, S. Gortler, and M. Cohen, "Unstructured lumigraph rendering," in *SIGGRAPH '01*, 2001.
- [63] T. Zhou, D.-P. Fan, M.-M. Cheng, J. Shen, and L. Shao, "Rgb-d salient object detection: A survey," *Computational Visual Media*, 2020.
- [64] E. Adelson and J. Bergen, "The plenoptic function and the elements of early vision," in *Computational Models of Visual Processing*. Cambridge: MIT Press, 1991.
- [65] M. Levoy and P. Hanrahan, "Light field rendering," in *SIGGRAPH '96*, 1996.
- [66] A. Agarwala, M. Dontcheva, M. Agrawala, S. Drucker, A. Colburn, B. Curless, D. Salesin, and M. Cohen, "Interactive digital photomontage," in *SIGGRAPH 2004*, 2004.
- [67] X. Lin, J.-L. Suo, G. Wetzstein, Q. Dai, and R. Raskar, "Coded focal stack photography," *Proceedings of the IEEE Conference on Computational Photography*, pp. 1–9, 2013.
- [68] W. Zhu, S. Liang, Y. Wei, and J. Sun, "Saliency optimization from robust background detection," in *Proceedings of the IEEE Conference on Computer Vision and Pattern Recognition*, 2014, pp. 2814–2821.
- [69] X. Shi, Z. Chen, H. Wang, D. Yeung, W. Wong, and W. Woo, "Convolutional lstm network: a machine learning approach for precipitation nowcasting," in *Proceedings of the Advances in Neural Information Processing Systems*, 2015, pp. 802–810.
- [70] L.-C. Chen, G. Papandreou, I. Kokkinos, K. Murphy, and A. Yuille, "Deeplab: Semantic image segmentation with deep convolutional nets, atrous convolution, and fully connected crfs," *IEEE Transactions on Pattern Analysis and Machine Intelligence*, vol. 40, pp. 834–848, 2018.
- [71] C. Yang, L. Zhang, H. Lu, X. Ruan, and M.-H. Yang, "Saliency detection via graph-based manifold ranking," in *Proceedings of the IEEE Conference on Computer Vision and Pattern Recognition*, 2013, pp. 3166–3173.
- [72] L. Wang, H. Lu, Y. Wang, M. Feng, D. Wang, B. Yin, and X. Ruan, "Learning to detect salient objects with image-level supervision," in *Proceedings of the IEEE Conference on Computer Vision and Pattern Recognition*, 2017, pp. 3796–3805.
- [73] R. Achanta, S. Hemami, F. J. Estrada, and S. Süsstrunk, "Frequency-tuned salient region detection," in *Proceedings of the IEEE Conference on Computer Vision and Pattern Recognition*, 2009.
- [74] F. Perazzi, P. Krähenbühl, Y. Pritch, and A. Sorkine-Hornung, "Saliency filters: Contrast based filtering for salient region detection," in *Proceedings of the IEEE Conference on Computer Vision and Pattern Recognition*, 2012, pp. 733–740.
- [75] D.-P. Fan, M.-M. Cheng, Y. Liu, T. Li, and A. Borji, "Structure-measure: A new way to evaluate foreground maps," in *Proceedings of the IEEE International Conference on Computer Vision*, 2017, pp. 4558–4567.
- [76] J. Zhao, Y. Cao, D.-P. Fan, M.-M. Cheng, X. yi Li, and L. Zhang, "Contrast prior and fluid pyramid integration for rgb-d salient object detection," in *Proceedings of the IEEE Conference on Computer Vision and Pattern Recognition*, 2019, pp. 3922–3931.
- [77] D.-P. Fan, C. Gong, Y. Cao, B. Ren, M.-M. Cheng, and A. Borji, "Enhanced-alignment measure for binary foreground map evaluation," in *Proceedings of the International Joint Conferences on Artificial Intelligence*, 2018.
- [78] Z. Wu, L. Su, and Q. Huang, "Stacked cross refinement network for edge-aware salient object detection," in *Proceedings of the IEEE International Conference on Computer Vision*, 2019, pp. 7263–7272.
- [79] M. Feng, H. Lu, and E. Ding, "Attentive feedback network for boundary-aware salient object detection," in *Proceedings of the IEEE Conference on Computer Vision and Pattern Recognition*, 2019, pp. 1623–1632.
- [80] X. Qin, Z. Zhang, C. Huang, C. Gao, M. Dehghan, and M. Jägersand, "Basnet: Boundary-aware salient object detection," in *Proceedings of the IEEE Conference on Computer Vision and Pattern Recognition*, 2019, pp. 7471–7481.

- [81] G. Li, Z. Liu, and H. Ling, "Icnnet: Information conversion network for rgb-d based salient object detection," *IEEE Transactions on Image Processing*, vol. 29, pp. 4873–4884, 2020.
- [82] A. Tsiami, P. Koutras, and P. Maragos, "Stavis: Spatio-temporal audio-visual saliency network," in *Proceedings of the IEEE Conference on Computer Vision and Pattern Recognition*, 2020, pp. 4765–4775.
- [83] D.-P. Fan, W. Wang, M.-M. Cheng, and J. Shen, "Shifting more attention to video salient object detection," in *Proceedings of the IEEE Conference on Computer Vision and Pattern Recognition*, 2019, pp. 8546–8556.
- [84] W. Zhao, F. Zhao, D. Wang, and H. Lu, "Defocus blur detection via multi-stream bottom-top-bottom network," *IEEE Transactions on Pattern Analysis and Machine Intelligence*, vol. 42, pp. 1884–1897, 2020.
- [85] J. Park, Y.-W. Tai, D. Cho, and I.-S. Kweon, "A unified approach of multi-scale deep and hand-crafted features for defocus estimation," in *Proceedings of the IEEE Conference on Computer Vision and Pattern Recognition*, 2017, pp. 2760–2769.
- [86] Y. Zeng, Y.-Z. Zhuge, H. Lu, L. Zhang, M. Qian, and Y. Yu, "Multi-source weak supervision for saliency detection," in *Proceedings of the IEEE Conference on Computer Vision and Pattern Recognition*, 2019, pp. 6067–6076.
- [87] M. Qian, J. Qi, L. Zhang, M. Feng, and H. Lu, "Language-aware weak supervision for salient object detection," *Pattern Recognit.*, vol. 96, 2019.
- [88] T. Chen, S. Liu, S. Chang, Y. Cheng, L. Amini, and Z. Wang, "Adversarial robustness: From self-supervised pre-training to fine-tuning," in *Proceedings of the IEEE Conference on Computer Vision and Pattern Recognition*, 2020, pp. 696–705.
- [89] A. Dai, C. Diller, and M. Nießner, "Sg-nn: Sparse generative neural networks for self-supervised scene completion of rgb-d scans," in *Proceedings of the IEEE Conference on Computer Vision and Pattern Recognition*, 2020, pp. 846–855.
- [90] Y. Zeng, P. Zhang, J. Zhang, Z. Lin, and H. Lu, "Towards high-resolution salient object detection," in *Proceedings of the IEEE International Conference on Computer Vision*, 2019, pp. 7233–7242.
- [91] Z. Cai and N. Vasconcelos, "Cascade r-cnn: High quality object detection and instance segmentation," *IEEE Transactions on Pattern Analysis and Machine Intelligence*, 2019.
- [92] K. Chen, J. Pang, J. Wang, Y. Xiong, X. Li, S. Sun, W. Feng, Z. Liu, J. Shi, W. Ouyang, C. C. Loy, and D. Lin, "Hybrid task cascade for instance segmentation," in *Proceedings of the IEEE Conference on Computer Vision and Pattern Recognition*, 2019, pp. 4969–4978.
- [93] S. Liu, L. Qi, H. Qin, J. Shi, and J. Jia, "Path aggregation network for instance segmentation," in *Proceedings of the IEEE Conference on Computer Vision and Pattern Recognition*, 2018, pp. 8759–8768.
- [94] G. Li, Y. Xie, L. Lin, and Y. Yu, "Instance-level salient object segmentation," in *Proceedings of the IEEE Conference on Computer Vision and Pattern Recognition*, 2017, pp. 247–256.
- [95] A. Karpathy and F.-F. Li, "Deep visual-semantic alignments for generating image descriptions," *IEEE Transactions on Pattern Analysis and Machine Intelligence*, vol. 39, pp. 664–676, 2017.
- [96] Y. Wei, W. Xia, J. Huang, B. Ni, J. Dong, Y. Zhao, and S. Yan, "Cnn: Single-label to multi-label," *ArXiv*, vol. abs/1406.5726, 2014.
- [97] X. Chen and A. Gupta, "Webly supervised learning of convolutional networks," in *Proceedings of the IEEE International Conference on Computer Vision*, 2015, pp. 1431–1439.
- [98] B. Lai and X. Gong, "Saliency guided dictionary learning for weakly-supervised image parsing," in *Proceedings of the IEEE Conference on Computer Vision and Pattern Recognition*, 2016, pp. 3630–3639.
- [99] X. Tian, K. Xu, X. Yang, B. Yin, and R. Lau, "Weakly-supervised salient instance detection," in *Proceedings of the Conference on British Machine Vision Conference*, vol. abs/2009.13898, 2020.
- [100] D.-P. Fan, G.-P. Ji, G. Sun, M.-M. Cheng, J. Shen, and L. Shao, "Camouflaged object detection," in *Proceedings of the IEEE Conference on Computer Vision and Pattern Recognition*, 2020, pp. 2774–2784.
- [101] Y. Xu, H. Nagahara, A. Shimada, and R. Taniguchi, "Transcut: Transparent object segmentation from a light-field image," in *Proceedings of the IEEE International Conference on Computer Vision*, 2015, pp. 3442–3450.